



SYNTHESIS AND CHARACTERISATION OF MATERIALS  
WITH POTENTIAL MULTIFERROIC BEHAVIOUR

by

RHYS D'SOUZA

A thesis submitted to  
The University of Birmingham  
for the degree of  
Master of Research

School of Chemistry  
The University of Birmingham  
September 2008

UNIVERSITY OF  
BIRMINGHAM

**University of Birmingham Research Archive**

**e-theses repository**

This unpublished thesis/dissertation is copyright of the author and/or third parties. The intellectual property rights of the author or third parties in respect of this work are as defined by The Copyright Designs and Patents Act 1988 or as modified by any successor legislation.

Any use made of information contained in this thesis/dissertation must be in accordance with that legislation and must be properly acknowledged. Further distribution or reproduction in any format is prohibited without the permission of the copyright holder.

## Acknowledgements

I would like to thank my supervisor, Professor Greaves for his indispensable advice and help during this project. When I started my project I did not know how to use all the laboratory facilities that were necessary for my project. Therefore, I would also like to take this opportunity to thank Jenny Readman for showing me how to use the D5000 and Fiona Coomer for helping me to take magnetic measurements on the PPMS and the SQUID. Special thanks goes to Ryan Bayliss for risking life and limb when operating the high pressure oxygen furnace. The friendly atmosphere on level 5 has made my work really enjoyable.

## Abstract

The ceramic method has been used to produce Aurivillius<sup>1</sup> phase materials,  $\text{Bi}_3\text{NbTiO}_9$  and  $\text{Bi}_4\text{Ti}_3\text{O}_{12}$ . The structures have been refined in  $A2_1am$  and  $Fmmm$  symmetry, respectively. In addition, the fractional co-ordinates of the constituent atoms of these materials has been calculated by Rietveld refinement.

A range of materials of general formula  $\text{Bi}_5\text{Fe}_{1+x}\text{Ti}_{3-x}\text{O}_{15}$  was produced with a value of  $x$  ranging from 0 to 2.5, which is higher than has been previously been reported. Attempts to produce  $\text{Bi}_5\text{Fe}_4\text{O}_{15}$ , with all the  $\text{Ti}^{4+}$  sites occupied by iron atoms proved unsuccessful. The space group of  $\text{Bi}_5\text{FeTi}_3\text{O}_{15}$  was determined to be  $A2_1am$ , however, the other 4-layer bismuth phases proved to difficult to characterise without more data.

Increasing the number of pseudo-perovskite layers from 2 to 3 to 4 (from  $\text{Bi}_3\text{NbTiO}_9$  to  $\text{Bi}_4\text{Ti}_3\text{O}_{12}$  to  $\text{Bi}_5\text{FeTi}_3\text{O}_{15}$  respectively) had a notable effect in increasing the size of the unit cell along the z-axis, going from  $c=25.192(1)\text{\AA}$  to  $c=32.785(1)\text{\AA}$  to  $c = 41.179(1)$

The magnetic properties of  $\text{Bi}_5\text{FeTi}_3\text{O}_{15}$ ,  $\text{Bi}_5\text{Fe}_2\text{Ti}_2\text{O}_{15}$  and  $\text{Bi}_5\text{Fe}_3\text{TiO}_{15}$  have been recorded, as part of an attempt to find multiferroic materials. The information collected would suggest that  $\text{Bi}_5\text{FeTi}_3\text{O}_{15}$  and  $\text{Bi}_5\text{Fe}_3\text{TiO}_{15}$  display some degree of anti-ferromagnetic behaviour, whereas  $\text{Bi}_5\text{Fe}_2\text{Ti}_2\text{O}_{15}$  appears to be a paramagnet.

Failure to produce  $\text{Bi}_5\text{MnTi}_3\text{O}_{15}$ , using methods outlined by other researchers<sup>2,3</sup>, raises doubts about the viability of manganese substitution into the bismuth-layer structure.

---

1B. Aurivillius, (1949), *Arkiv for Kemi*, Volume 1, Iss. 6, p499-512

2S. Ahn, Y. Noguchi, M. Miyayama, T. Kudo, (2000), *Materials Research Bulletin*, Volume 35, p825-834

3M.M. Kumar, A. Srinivas, G.S. Kumar, S.V. Suryanarayana, (1997), *Solid State Communications*, Volume 104, Number 12, p741-746

# Contents

<b>1. Introduction</b>	<b>1</b>
1.1 Multiferroics	1
1.2 Aurivillius Phases	7
1.3 B-Cation Substitution in Bismuth Titanates	11
1.4 Aims of this Project	14
<b>2. Experimental</b>	<b>15</b>
2.1 Preparation Techniques	15
2.1.1 Preparation of $\text{Bi}_3\text{NbTiO}_9$	16
2.1.2 Preparation of $\text{Bi}_4\text{Ti}_3\text{O}_{12}$	16
2.1.3 Preparation of $\text{Bi}_5\text{Fe}_{1+x}\text{Ti}_{3-x}\text{O}_{15}$	17
2.1.4 Preparation of $\text{Bi}_5\text{Fe}_{2.5}\text{Ti}_{1.5}\text{O}_{15}$ and $\text{Bi}_5\text{Fe}_3\text{TiO}_{15}$	17
2.2 Characterisation Techniques	18
2.2.1 X-ray Diffraction and Rietveld Refinement	18
2.2.1.1 X-ray Diffraction	18
2.2.1.2 XRPD Analysis and Rietveld Refinement	22
2.2.2 Physical Properties Measurement System	26
2.2.3 Superconducting Quantum Interference Devices (SQUID)	27
<b>3. Results and Discussion</b>	<b>31</b>
3.1 $\text{Bi}_3\text{NbTiO}_9$ Characterisation	31
3.1.1 $\text{Bi}_3\text{NbTiO}_9$	31
3.1.2 Characterisation of $\text{Bi}_3\text{NbTiO}_9$	31
3.2 $\text{Bi}_4\text{Ti}_3\text{O}_{12}$ Characterisation	34
3.2.1 $\text{Bi}_4\text{Ti}_3\text{O}_{12}$	34
3.2.2 Characterisation of $\text{Bi}_4\text{Ti}_3\text{O}_{12}$	34

3.3 Characterisations of $\text{Bi}_5\text{Fe}_{x+1}\text{Ti}_{3-x}\text{O}_{15}$	37
3.3.1 $\text{Bi}_5\text{FeTi}_3\text{O}_{15}$	37
3.3.1.1 Characterisation of $\text{Bi}_5\text{FeTi}_3\text{O}_{15}$	37
3.3.2 Alternative Synthesis of $\text{Bi}_5\text{FeTi}_3\text{O}_{15}$	41
3.3.3 $\text{Bi}_5\text{Fe}_{x+1}\text{Ti}_{3-x}\text{O}_{15}$	42
3.3.3.1 Characterisations of $\text{Bi}_5\text{Fe}_{x+1}\text{Ti}_{3-x}\text{O}_{15}$	42
3.3.3.2 Characterisation of $\text{Bi}_5\text{Fe}_{1.5}\text{Ti}_{2.5}\text{O}_{15}$	43
3.3.4 Synthesis of $\text{Bi}_5\text{Fe}_{2+x}\text{Ti}_{2-x}\text{O}_{15}$	44
3.3.4.1 Magnetic Characterisation of $\text{Bi}_5\text{Fe}_2\text{Ti}_2\text{O}_{15}$ and $\text{Bi}_5\text{Fe}_3\text{TiO}_{15}$	45
3.3.5 Attempted Synthesis of $\text{Bi}_5\text{Fe}_4\text{O}_{15}$	47
3.4 Attempted Synthesis and Characterisation of $\text{Bi}_5\text{Mn}_{1+x}\text{Ti}_{3-x}\text{O}_{15}$	48
4. Conclusions and Further Work	51
4.1 Conclusions	51
4.2 Further Work	52
5. References	54
Appendix A: X-ray Powder Diffraction Patterns	
Appendix B: Mössbauer Spectroscopy	

## **Section 1: Introduction**

### **1.1 Multiferroics**

This project reports the study of a series of layered bismuth compounds, with structures related to Aurivillius phases<sup>1</sup> The main aim of this project was to achieve significant substitution of magnetic ions into the aforementioned Aurivillius phases, which will hopefully then have the potential to display multiferroic properties.

Multiferroic materials are commonly defined as those which simultaneously display the properties of ferroelectricity and some form of magnetic ordering, either ferromagnetism or anti-ferromagnetism. Some have included ferroelasticity as one of the properties of multiferroic materials, however this property is not included in this study.

Ferroelastic, ferroelectric and ferromagnetic properties can all have their behaviour described by a phenomenon known as hysteresis. In fact, the reason that the ferro- prefix is common for all three of these separate properties has its roots in the fact that all properties share hysteresis behaviour. A hysteresis loop shows how two parameters are related, such as the relationship between strain and mechanical stress displayed by ferroelastic materials. Hysteresis behaviour can be described graphically (Figure 1).

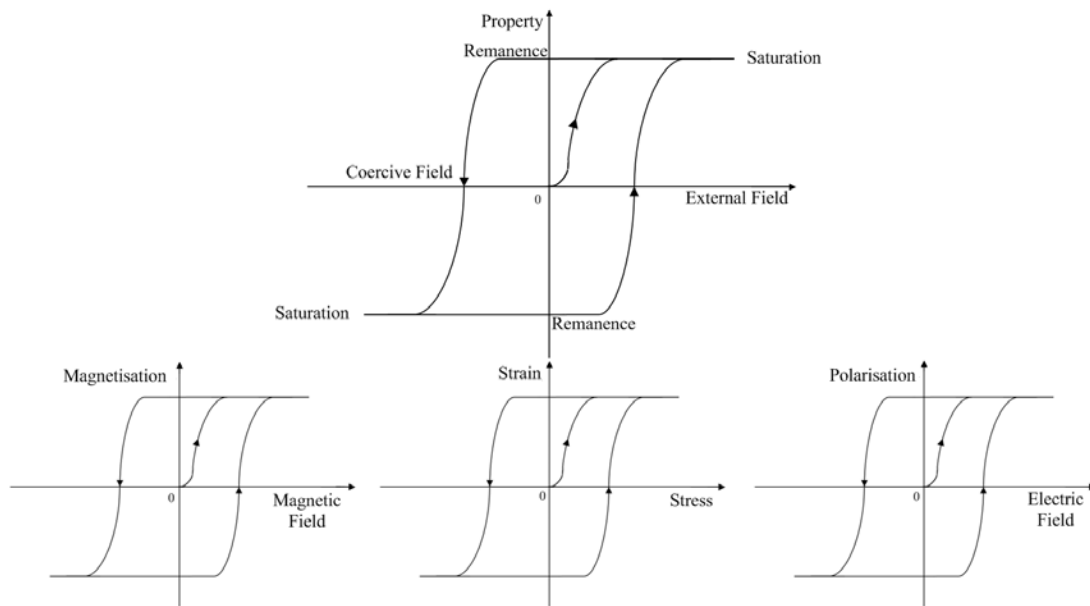


**Figure 1:** Diagram of hysteresis behaviours. Top: General graph of hysteresis, with the Property plotted against the Coercive Field, with the features of Saturation, Coercive Field and Remanence marked. Bottom: the property and coercive fields for, from left to right, Ferromagnetic, Ferroelastic, Ferroelectric.

At the origin (point (0,0), at the centre of the graph), all the domains within the material are aligned randomly. In all cases, as the external field is increased, the domains within the material respond. Prior to the initial polarization of the domains within the material the only way to drive the domains back to the unaligned position at the origin is to apply a field in the opposing direction. Once the initial polarisation has been completed, the external field can only drive the polarisation up to the saturation point. At the saturation point, all the domains have been aligned and the polarisation of the material can increase no further.

Once saturation has been achieved, removal of the external field can no longer send the polarisation back to the origin where all the domains are unaligned. Instead, removing the external field will still leave the material with a remnant polarisation, which is known as the remanence. As the direction of the field is reversed, the domains within the material can be reversed until the polarisation is saturated, but this

time saturation is achieved in the negative direction. The coercitivity of the material relates to the coercive field, that is, the magnitude of the field that is required to negate the behaviour induced in the material, after saturation.

If the external field is cycled between the positive and negative directions, with a sufficiently powerful field, the polarisation of the material will rotate around the hysteresis loop in an anti-clockwise direction. The area of the hysteresis loop is proportional to the energy absorbed for each cycle of the hysteresis loop.

Smaller hysteresis loops are described as 'soft', where the polarisation of the material can be switched comparatively easily. Soft hysteresis finds uses in applications where the alignment has to be changed quickly, for instance transistors use soft ferromagnets. Hysteresis loops described as 'hard' have much larger loops and consequently altering the polarisation of these materials requires a greater amount of energy. Hard hysteresis is useful for applications where a material has to be able to retain its alignment for a significant amount of time. Obviously, not all materials display either hard or soft hysteresis, and there are plenty of uses for materials that display neither hard nor soft hysteresis.

Ferroelasticity is the property of displaying a spontaneous strain when stress is applied. The property of ferroelasticity was first recognised in 1969<sup>2</sup>. A ferroelastic crystal is able to adopt two or more stable orientation states, specifically in the absence of any mechanical stress or electric field. A ferroelastic material also has the ability to convert between these multiple orientation states whenever mechanical stress is applied<sup>3</sup>.

The property of ferroelectricity refers to a spontaneous polarization that can be altered by an applied electrical field. Ferroelectricity occurs when cations are displaced from their ideal sites in the unit cell, creating domains of dipoles which can then be manipulated by an electric field.

When an electric field,  $E$ , is applied there is polarisation,  $P$ , which aligns the domains in the ferroelectric material. More importantly, after the electrical polarizations of many unit cells are aligned there exists a remanent polarization, so the domains remain aligned, even when the electrical field is removed, which leads to hysteresis behaviour.

The perovskite structure is typified by large A cations at the corners of the unit cell with a smaller B cation at the centre of an octahedron of oxygen anions in the middle of the unit cell (Figure 2). In ferroelectric perovskites the central B cation moves from its ideal position, giving rise to a dipole moment. Ferroelectricity can exist in perovskite and pseudo-perovskite structures due to ligand field stabilization, as electron density from the oxygen 2p

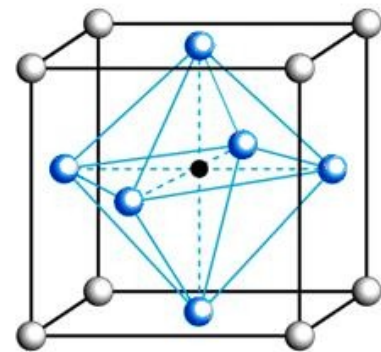


**Figure 2:** An example of the perovskite unit cell (centred on B), with the blue spheres representing oxygen, black spheres representing the B cation and the white sphere representing the A cation.

state can be

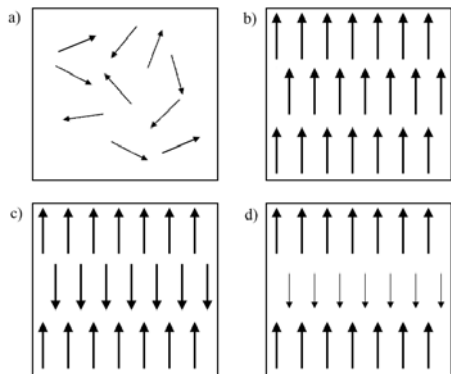


**Figure 3:** Ordering of dipoles in magnetic materials. a) Paramagnetism, b) Ferromagnetism, c) Anti-ferromagnetism, d) Ferrimagnetism.

donated to the formally vacant d-sub-shells of the cation as it moves from its undistorted position.

Ferrimagnetism (d in Figure 3) occurs in situations where overall there is a net dipole,

despite having oppositely aligned dipoles. Paramagnetic (a in Figure 3) materials have no magnetic ordering at all. Magnetic ordering in multiferroic crystals typically refers to ferromagnetism (b in Figure 3), but sometimes the definition of multiferroic is extended to include anti-ferromagnetism (c in Figure 3). Ferromagnetism and anti-ferromagnetism are derived from the existence of unpaired electrons, the individual electron spins coordinating in a parallel or anti-parallel fashion, giving rise to ferromagnetism or anti-ferromagnetism, respectively.

There is a stark contrast between the prerequisites of ferroelectricity, which has vacant valence shells, rather than the unpaired electrons which are required for magnetic dipoles. This apparent dichotomy between ferroelectric and ferromagnetic or anti-ferromagnetic properties, has led to several papers being written on the existence of multiferroic behaviour. One such paper is Hill and Filippetti's '*Why are there any magnetic ferroelectrics?*'<sup>4</sup> which draws heavily on work by H. Schmid, among others. Schmid<sup>5</sup> pointed out that of 122 Shubnikov-Heesch point groups, only 13 could be simultaneously ferroelectric and ferromagnetic<sup>6,7</sup> and only 8 could display ferroelectricity and antiferromagnetism<sup>6</sup>.

As ferroelectricity is caused by the existence of a dipole, a unit cell needs to be non-centrosymmetric, if it is to display ferroelectricity. Meanwhile, for magnetic ordering to exist in a crystal it requires that the unit cell does not include time inversion as a component of its space group<sup>8</sup>. K. Aizu contributed greatly to finding multiferroic space groups, by identifying a range of space groups which display multiferroic behaviour<sup>9</sup>.

The reason for the interest in multiferroic materials is due to their potential use in commercial applications. The ability to utilise both magnetic and electric polarisation opens many options in the field of data storage. For instance, using the different hysteresis behaviours allows multiple memory state components, capable of storing data in both the magnetic and the electric polarisations. Current memory systems only allow data to be stored in either polarisation, but not both, depending on the type of memory being used. Another possibility would be that multiferroic materials would provide a pathway to non-volatile memory systems (NVRAM) that would allow data to be stored, even in situations where the power supply is interrupted<sup>10</sup>.

## 1.2 Aurivillius Phases

The paper that introduced the structure that came to be known as the Aurivillius phase was written by Aurivillius and published in 1949<sup>1</sup>. The Aurivillius phase forms the cornerstone of this project. The Aurivillius phase has the general formula  $[\text{Bi}_2\text{A}_{n-1}\text{B}_n\text{O}_{3n+3}]$ <sup>11</sup>. Structurally, the

Aurivillius phase is typified by fluorite-like  $[\text{Bi}_2\text{O}_2]^{2+}$  interspersed between perovskite-like  $[\text{A}_{n-1}\text{B}_n\text{O}_{3n+1}]^{2-}$  layers (where  $n$  represents the number of layers)<sup>12</sup>, an example is

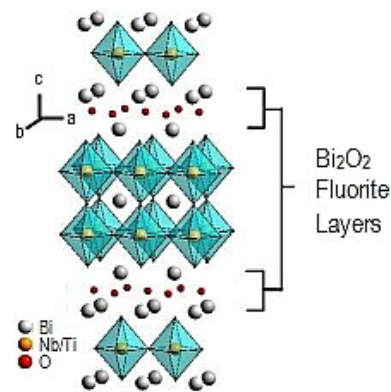


**Figure 4:** Bi<sub>3</sub>NbTiO<sub>9</sub>-  
An example of the  
Aurivillius Phase  
(A= Bi, B=Nb/Ti, n=2)

shown in Figure 4. Having an  $n$  of infinity would be equivalent to a perovskite structure. Typically, the A position is taken by an electropositive atom (either mono-, di- or tri-valent ions, or possibly a mixture thereof), while B is generally a transition metal with a  $d^0$  configuration.

The first ferroelectric material with a layered structure based on fluorite-like  $[\text{Bi}_2\text{O}_2]^{2+}$  layers was  $\text{PbBi}_2\text{Nb}_2\text{O}_9$ , discovered by Smolenskii, Isupov and Agranovskaya<sup>13</sup>. Several years later, E.C. Subbarao listed a large number of Aurivillius phases that displayed ferroelectricity, sparking a great deal of interest in the field<sup>14</sup>.

Another paper of note is a study which focussed on the causes for ferroelectricity in the Aurivillius phase; Newnham, *et al.* sought to find a structural explanation for the large number of ferroelectric Aurivillius phase materials. Their work postulated that the potential spontaneous polarisation of Aurivillius phases was

largely due to the displacement of octahedral cations (B in the general structure) from their ideal position at the centre of oxygen octohedra<sup>15</sup>.

While this work was influential in attempting to find a structural cause for the high proportion of ferroelectric Aurivillius phases, it was superseded by a paper suggesting a revised structure for  $\text{Bi}_3\text{NbTiO}_9$ . Thompson, *et al.*, later reviewed the structure and concluded that it was the displacement of  $\text{Bi}^{3+}$ , rather than octahedral cations that was the major contributing factor to ferroelectric behaviour<sup>16</sup>. Thompson, *et al.* later showed that this was also true of other Aurivillius phase crystals, challenging previous notions<sup>17</sup>. This theory is also supported by research into multiferroic perovskite structures, such as  $\text{BiMnO}_3$ , and  $\text{BiFeO}_3$ , whose ferroelectric behaviour is also the result of A cation displacement<sup>18</sup>.

The likely source for magnetic ordering in Aurivillius phases would be due to an exchange mechanism. Superexchange gives rise to magnetic ordering<sup>19</sup>. While the electrons remain localised, the superexchange mechanism constitutes a virtual metal-metal charge transfer (Figure 5). If one of the transition metal ions transfers electron density from its d-electron orbitals onto the oxygen 2p sub-shell, then electron density is consequently transferred onto the next transitional metal ion. The second metal ion

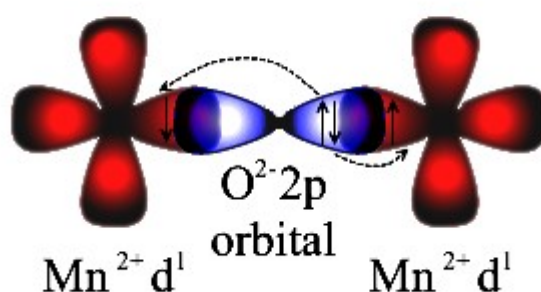


**Figure 5:** Diagram of the anti-ferromagnetic superexchange mechanism.

must have an opposite electron spin, otherwise superexchange cannot occur, as the electron density cannot be transferred. As the transition metal ions have opposite spin, this gives rise to anti-ferromagnetic ordering.

However, under certain conditions, it is possible for a superexchange mechanism to lead to a ferromagnetically ordered material. This can be achieved in several situations, such as superexchange between two different ions (Figure 6):

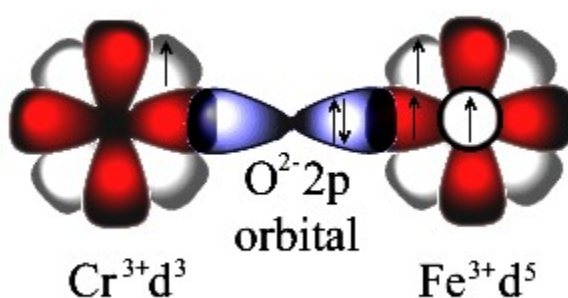


**Figure 6:** Diagram of a ferromagnetic superexchange mechanism.

In  $d^4$  and  $d^9$  metal ions, regular Jahn-Teller distortions can lead to magnetic ordering. This is because the removal of the degeneracy of the  $e_g$  states, increases the stability of these metal ions. The Jahn-Teller distortion, leads to the cation shifting from an octahedral co-ordination, to a tetragonally distorted octahedron. This can influence ferromagnetic ordering, as in  $\text{Rb}_2\text{CrCl}_4$ <sup>20</sup>, or anti-ferromagnetic ordering, as in  $\text{LaMnO}_3$ <sup>21</sup>. This is because in  $\text{LaMnO}_3$  the ferromagnetic planes form in an alternating pattern, and this anti-parallel arrangement of ferromagnetic planes leads to an overall anti-ferromagnetic ordering<sup>22</sup>. Magnetic ordering in crystal structures can also occur via  $\pi$ -interactions that involve the  $p_x$  and  $p_y$  orbitals of the intermediate anion.

Another mechanism for magnetic ordering is known as double exchange. Double exchange allows for the movement of electrons between ferromagnetically ordered transition metal ions via oxygen (Figure 7).

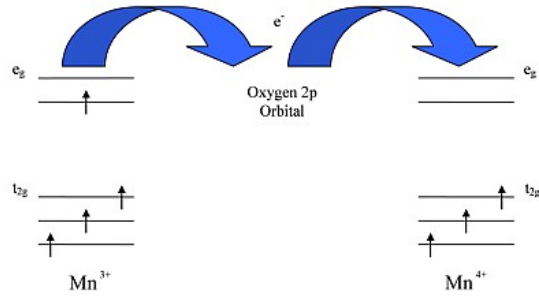


**Figure 7:** Diagram of the double exchange mechanism

Due to the strong orbital interaction between the  $t_{2g}$  and the  $e_g$  orbitals, double exchange can only occur when the Coulomb repulsion is minimised, i.e. the  $t_{2g}$  electrons on cation B are aligned parallel to the electrons on cation A. The parallel alignment of these electrons leads to ferromagnetic ordering.

### 1.3 B-Cation Doping in Bismuth Titanates

In bismuth titanate,  $\text{Bi}_4\text{Ti}_3\text{O}_{12}$ , the  $\text{Bi}^{3+}$  cation has been replaced, at least to some extent, by a variety of lanthanoids, including  $\text{La}^{3+}$ ,  $\text{Pr}^{3+}$ ,  $\text{Nd}^{3+}$ ,  $\text{Sm}^{3+}$ ,  $\text{Eu}^{3+}$ ,  $\text{Gd}^{3+}$ ,  $\text{Tb}^{3+}$ ,  $\text{Dy}^{3+}$ ,  $\text{Ho}^{3+}$ ,  $\text{Er}^{3+}$ ,  $\text{Tm}^{3+}$ ,  $\text{Yb}^{3+}$ ,  $\text{Lu}^{3+}$ . As the radius of the dopant decreases, the amount by which it can substitute for  $\text{Bi}^{3+}$  also decreases.

As well as lanthanoids, alkali metals,  $\text{Na}^+$ ,  $\text{K}^+$ ,  $\text{Li}^+$ , have been used as dopants for bismuth ions to induce piezoelectric behaviour in Aurivillius phase materials. The piezoelectric behaviour of the alkali metal substituted materials can be further improved by doping with cerium oxide<sup>23</sup>.

Substituting a metal cation for  $\text{Ti}^{4+}$  in the bismuth titanate structure requires certain criteria to be met. The first consideration is the balancing of electronic charges. Although only ions with a 4+ charge can be switched on a like-for-like basis, by mixing dopants, it is possible to use cations with various oxidation states. For instance, doping may involve a mixture of 3+ and 5+ ions, or a variety of A cation substitutions to balance the charges involved.

The second consideration for substitution is the size of the ionic radius. The

tolerance factor ( $t = \frac{r_a + 1.40}{\sqrt{2}(r_b + 1.40)}$ ) of the pseudo-perovskite layer is a smaller range than that of a standard perovskite (0.81-0.93 as opposed to 0.77-1.01<sup>24</sup>). This means that the ionic radius of the octahedral cation must be within a range of 0.58-0.65Å. The lower limit of this range is caused by the loss of stability of the pseudo-perovskite structure, due to the internal strain induced when attempting to fit

smaller cations. Meanwhile, the upper limit is a result of the potential mismatch in size between the  $(A_{m-1}B_mO_{3m+1})$  pseudo-perovskite and  $(Bi_2O_2)^{2+}$  layers; if the layers cannot align then a stable structure cannot be formed<sup>25</sup>.

This factor is seen in the cases of  $Ge^{4+}$ , whose ionic radius of 0.54 Å is outside the range that can be substituted, as it is too small. Other examples include  $Sn^{4+}$ ,  $Hf^{4+}$  and  $Zr^{4+}$ , whose radii of 0.69 Å, 0.71 Å and 0.72 Å respectively, put them outside the appropriate range, but this time at the opposite end of the scale, being too large for substitution.

An alternative to A site or B site cation substitution would be double substitution. Examples of double substitution, where both the bismuth and titanium cations are substituted, include the substitution of  $Ca^{2+}$ ,  $Sr^{2+}$ ,  $Ba^{2+}$  and  $Pb^{2+}$  for bismuth, with a complementary substitution of titanium for either niobium or tantalum to balance the charges involved.

The relationship between ionic radius and lattice  $a$  parameter for the layer has been observed to be  $a = 0.6r_A + 1.33r_B + 2.36\text{Å}$ . Ideally, the parameter,  $a$ , is as close to the lattice parameter of the  $Bi_2O_2$  layer (3.80 Å) as possible. Any  $a$  calculated to be over 4 Å causes enough internal strain to destabilise the structure<sup>25</sup>. From the coefficients, it is quite clear that the size of the B site cation is a more significant factor in regards to stability than the A site cation.

Therefore,  $Co^{3+}$  (0.61 Å),  $Cr^{3+}$  (0.615 Å),  $Fe^{3+}$  (0.645 Å),  $Fe^{4+}$  (0.585 Å) and  $Mn^{3+}$  (0.645 Å) have potential for substantial substitution. Compounds that have been

synthesised include  $\text{Bi}_4\text{Ti}_{(3-2x)}\text{Nb}_x\text{Fe}_x\text{O}_{12}$  ( $x= 0.25, 0.5$ )<sup>26</sup> and  $\text{Bi}_4\text{Ti}_{(3-x)}\text{Mn}_x\text{O}_{12}$  ( $x= 0.05, 0.1, 0.2$ )<sup>27</sup>.

Another possibility is to combine  $\text{Bi}_4\text{Ti}_3\text{O}_{12}$  and relatively easy to form  $\text{Bi}_5\text{Ti}_3\text{BO}_{15}$  (where B= Mn, Fe, Cr, etc.) through perovskite layer intergrowth, where the perovskite layer alternates between the two Aurivillius phases.

In this way, two Aurivillius phases can be combined to make a larger layered structure, as long as the constituent phases differ in size by only one layer, e.g.  $(\text{Bi}_2\text{O}_2)(\text{A}_{m-1}\text{B}_m\text{O}_{3m+1}) + (\text{Bi}_2\text{O}_2)(\text{A}'_m\text{B}'_{m+1}\text{O}_{3m+4}) = \text{Bi}_4\text{A}_{2m-1}\text{B}_{2m+1}\text{O}_{6m+9}$ <sup>28</sup>. This intergrowth method has been

used to create  $\text{Bi}_9\text{Ti}_6\text{CrO}_{27}$ , amongst others<sup>29</sup>. With careful planning it is possible to use intergrowth

structures (Figure 8), to improve the properties of existing Aurivillius phase materials by creating stronger hysteresis<sup>30</sup>.

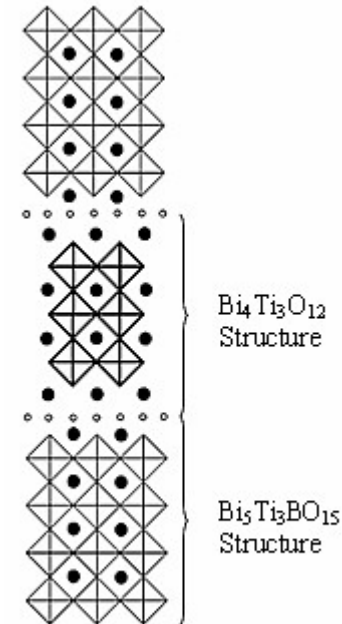


**Figure 8:** Diagram of an intergrowth structure.

## 1.4 Aims of this Project

This thesis will focus on several key areas:

- The attempt to form and characterise  $\text{Bi}_3\text{TiNbO}_9$ .
- The attempt to form and characterise  $\text{Bi}_4\text{Ti}_3\text{O}_{12}$ .
- The attempted synthesis and characterisation of  $\text{Bi}_5\text{Fe}_{1+x}\text{Ti}_{3-x}\text{O}_{15}$  compounds.

These compounds feature higher Fe content than has previously been reported.

The characterisation of these materials also includes the magnetic characterisation, to indicate possible multiferroic behaviour.

- An attempt to synthesise  $\text{Bi}_5\text{Mn}_{1+x}\text{Ti}_{3-x}\text{O}_{15}$  using similar methods to the production of  $\text{Bi}_5\text{Fe}_{1+x}\text{Ti}_{3-x}\text{O}_{15}$  compounds.

## **Section 2: Experimental**

### **2.1 Preparation Techniques**

The means by which all samples were prepared is known as the ceramic method. The ceramic method involves the grinding of stoichiometric quantities of powders to form a homogeneous mixture. Although grinding can be done by mechanical means, the grinding used in this thesis was done by hand, using a mortar and pestle. The various reagents used were all 99.999% oxide powders from Sigma-Aldrich.

The homogeneous mixture was then heated in a furnace. Typically, several different heating stages using different temperatures, heating rates, and durations were used to achieve the desired effect. In between heat treatments the mixture was ground again to refresh the reaction interfaces between the various powders. This ensures the best rate of reaction, as it improves the surface area and mobility of the reagents.

Reaction conditions were altered by using oxygen and 10% hydrogen/90% nitrogen gas when appropriate. The  $\text{Bi}_5\text{Fe}_{1.5}\text{Ti}_{2.5}\text{O}_{15}$  and  $\text{Bi}_5\text{Fe}_2\text{Ti}_2\text{O}_{15}$  were both treated using a high oxygen pressure furnace. In the high oxygen pressure furnace, oxygen is supplied to a regulator at 220 bars of pressure. The oxygen is then pumped into the furnace, creating a much higher overall pressure, due to the higher temperature.

Using the combined gas law the pressure inside the furnace can be calculated. The combined gas law, is itself, an amalgam derived of Boyle's Law, Charles's Law and Guy-Lussac's Law. Each of these thermodynamic laws demonstrates how one variable is affected by change in the other. For instance, Boyle's Law shows the relationship between pressure and volume, Charles's Law

shows the relationship between volume and temperature and Gay-Lussac's Law demonstrates how pressure and temperature are related. The combined gas law is:

$$\frac{P_1 V_1}{T_1} = \frac{P_2 V_2}{T_2}$$

As the volume of the furnace chamber remains constant, i.e.  $V_1=V_2$ , so this variable can be removed from both sides of the equation. This gives us:

$$\frac{P_1}{T_1} = \frac{P_2}{T_2}$$

The initial pressure,  $P_1$ , is 220 bar, the initial temperature,  $T_1$ , is room temperature at 298 K. The temperature inside the furnace increases to 1123 K, increasing the furnace pressure to 829 bar.

### **2.1.1 Preparation of $\text{Bi}_3\text{NbTiO}_9$**

To prepare  $\text{Bi}_3\text{NbTiO}_9$ , stoichiometric amounts of  $\text{Bi}_2\text{O}_3$ ,  $\text{Nb}_2\text{O}_5$  and  $\text{TiO}_2$  were ground together, for 30 minutes in a mortar and pestle, before being placed in a furnace. The homogeneous ground mixture was then fired in a Carbolite CWF 1300 furnace at 1160°C for 10 hours. This temperature was chosen due to work performed showing the relationship between sintering temperature and percentage yield<sup>31</sup>.

### **2.1.2 Preparation of $\text{Bi}_4\text{Ti}_3\text{O}_{12}$**

Bismuth titanate was prepared in a similar manner to  $\text{Bi}_3\text{NbTiO}_9$ , but without  $\text{Nb}_2\text{O}_5$  as a reagent. In addition, for bismuth titanate the stoichiometric amounts of  $\text{Bi}_2\text{O}_3$  and  $\text{TiO}_2$  in the furnace were only heated to 1000°C for 10 hours, the same duration as the synthesis of  $\text{Bi}_3\text{NbTiO}_9$ .

### **2.1.3 Preparation of $\text{Bi}_5\text{Fe}_{1+x}\text{Ti}_{3-x}\text{O}_{15}$**

The majority of the various samples of  $\text{Bi}_5\text{Fe}_{1+x}\text{Ti}_{3-x}\text{O}_{15}$  (with  $x$  ranging from 0 to 1 and increasing in increments of 0.1) were prepared with two separate firings of stoichiometric amounts of  $\text{Bi}_2\text{O}_3$ ,  $\text{Fe}_2\text{O}_3$  and  $\text{TiO}_2$ . The two firings took place at  $850^\circ\text{C}$  in oxygen at atmospheric pressure, with the first firing lasting for 10 hours, then the second lasting for 8 hours.

The exceptions to this method are  $\text{Bi}_5\text{FeTi}_3\text{O}_{15}$ ,  $\text{Bi}_5\text{Fe}_{1.1}\text{Ti}_{2.9}\text{O}_{15}$  and  $\text{Bi}_5\text{Fe}_{1.6}\text{Ti}_{2.4}\text{O}_{15}$ . The sample of  $\text{Bi}_5\text{FeTi}_3\text{O}_{15}$  was formed by a single 12 hour firing at  $1050^\circ\text{C}$  in air. The sample of  $\text{Bi}_5\text{Fe}_{1.1}\text{Ti}_{2.9}\text{O}_{15}$  was formed by a 12 hour firing at  $1050^\circ\text{C}$  in air, followed by two firings in oxygen at atmospheric pressure at  $850^\circ\text{C}$ , first for 10 hours and then for 8 hours. To prepare  $\text{Bi}_5\text{Fe}_{1.6}\text{Ti}_{2.4}\text{O}_{15}$ , following two separate firings at  $850^\circ\text{C}$  in oxygen at atmospheric pressure, first for 10 hours, then for 8 hours; it was found that an initial 8 hour firing under the same reaction conditions was necessary.

### **2.1.4 Preparation of $\text{Bi}_5\text{Fe}_{2.5}\text{Ti}_{1.5}\text{O}_{15}$ and $\text{Bi}_5\text{Fe}_3\text{TiO}_{15}$**

For these samples, stoichiometric amounts of  $\text{Bi}_2\text{O}_3$ ,  $\text{Fe}_2\text{O}_3$  and  $\text{TiO}_2$  were used. The pre-sintering was carried out at  $800^\circ\text{C}$  for 12 hours, while sintering was carried out at  $850^\circ\text{C}$  for 12 hours. A fifteen minute period of grinding with a mortar and pestle took place between the pre-sintering and sintering phases. It is important to note that both the heat treatments took place in air, rather than in oxygen (as was used previously) therefore, for future reference, those materials may not require an atmosphere of oxygen when being fired, although this is unknown without any further evidence.

## **2.2 Characterisation Techniques**

### **2.2.1 X-ray Diffraction and Rietveld Refinement**

#### **2.2.1.1 X-ray Diffraction**

The primary method used for determining the size and symmetry of unit cells is X-ray diffraction. Crystalline structures are comprised of many unit cells, a unit cell being the smallest arrangement of atoms that can be used to recreate the crystal purely by translational displacements. As the atoms form repeating units in space, it can be related to a space lattice of points, known as a Bravais lattice. In three dimensions, there are a total of fourteen distinct Bravais lattices<sup>32</sup>.

Due to the periodicity of the repeating unit cells, there are repeating planes made up of atoms, whose electron density has the effect of scattering X-rays. A crystal lattice will have many sets of planes, each with their own interplanar spacing. These sets of planes act as a diffraction grating for X-rays of the appropriate wavelength.

A plane is defined by its Miller indices, a set of three values, (hkl), which give the reciprocal lattice vector that lies perpendicular to the plane in question. Each plane has a unique reciprocal lattice vector, so an individual unit cell can be determined by its Miller indices.

If we consider two parallel planes inside a crystal, which are both incident to two monochromatic X-rays (as seen in Figure 9); the path difference for wave **b**, as opposed to wave **a**, has to be equal to an integer number of wavelengths ( $n\lambda$ ) for it to lead to constructive interference. The path difference between **a** and **b** is equal to  $2l$ .

As  $d$  is the hypotenuse of a right-angled triangle made by the perpendicular to the plane and the vectors of waves  $\mathbf{a}$  and  $\mathbf{b}$ ,  $l$  is closely related to  $d$ , the distance between the planes, given by the equation:

$$l = d \sin \theta$$

From this information, Bragg's law can be calculated, which is used to interpret the XRD data:

$$2 d \sin(\theta) = n \lambda$$

Where

$d$  = Distance between planes (Å)

$\theta$  = Angle of reflection

$n$  = Order of Diffraction (an

integer, which can be controlled

for calculation purposes)

$\lambda$  = Wavelength of source

(1.5406 Å)

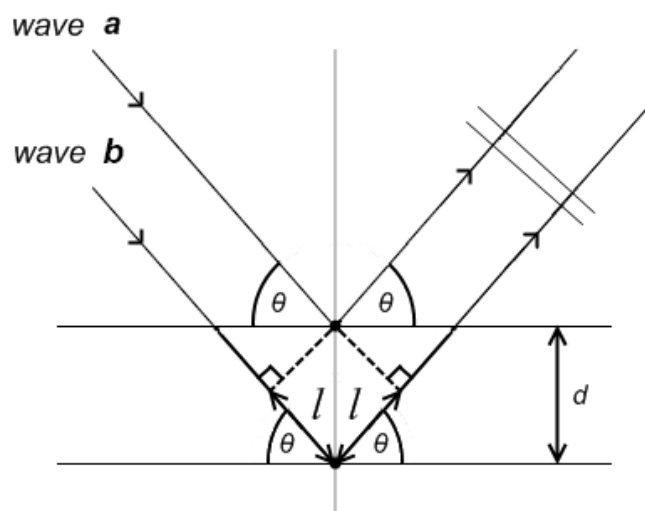


**Figure 9:** Diagram showing the interaction between two X-rays (waves  $\mathbf{a}$  and  $\mathbf{b}$ ) and two parallel planes, separated by distance  $d$ , to demonstrate Bragg's Law

As the value of  $\lambda$  is known,  $n$  is set to 1 and the  $\theta$  values are the data collected by XRD, it is possible to calculate the  $d$ -spacing. This in turn, allows the determination of the unit cell parameters, symmetry, atomic positions and unit cell size.

The intensity of the reflection depends on a variety of different factors and is given by:

$$I_{hkl} = m F_{hkl}^2 A L_p$$

Where  $m$  represents the multiplicity of the unit cell,  $F_{hkl}$  is the structure factor,  $A$  represents absorption and  $L_p$  is the Lorentzian polarisation factor. Absorption increases for heavier atoms. The structure factor,  $F_{hkl}$ , takes into account the resultant effect of wave scattering by all the atoms in the unit cell, in the (hkl) direction. It is given by the following equation for  $n$  atoms in a unit cell:

$$F_{hkl} = \sum_1^n f_n \exp[2\pi i(hx_n + ky_n + lz_n)] \exp\left[\frac{-B_n \sin^2 \theta}{\lambda^2}\right]$$

The factor  $f_n$  refers to the scattering factor, a measure of how effectively an atom scatters X-rays, largely based on the number of electrons the atom contains. The position of the atom is given by its coordinates,  $x_n, y_n, z_n$ . The Debye-Waller temperature factor has the symbol  $B_n$ , which is related to the displacement of an atom.

$$B_n = 8\pi^2 U$$

Where  $U$  is the mean square amplitude of atom vibration, which is given in  $\text{\AA}^2$ . With all this information, X-ray diffraction is a powerful technique which can tell us a great deal about the unit cell.

There are two different types of X-ray diffraction, X-ray powder diffraction (XRPD) and single crystal diffraction. Single crystal data allows the user to accurately determine each hkl reflection and its intensity. Analysis of these data allow the precise determination of the space group and thus, its atomic positions and lattice parameters. The major drawback however, is that single crystal data require the growth of a large crystal, which in practise can be quite difficult.

X-ray powder diffraction, as the name suggests, allows the use of powders to derive the structural information, which are easier to prepare as opposed to single crystals. The XRPD data can be compared to a database containing a large number of

powder diffraction files, which allows for relatively easy identification of the different phases that are present in the powder sample. The database contains data collated by the International Centre for Diffraction Data<sup>33</sup>.

All XRPD data in this thesis are from a Siemens D5000 diffractometer using Cu  $K\alpha_1$  radiation ( $\lambda = 1.5406\text{\AA}$ ) with a Ge primary beam monochromator and position sensitive detector. The X-rays are generated by bombarding Cu with high energy electrons. This causes the Cu to lose an electron from the K shell (1s orbital), creating a vacancy. This partial vacancy of the K shell leads to the transition of an electron from either the 2p or 3p shells. This transition leads to the emission of radiation in the X-ray region of the electromagnetic spectrum.

For Cu, three intense X-ray wavelengths arise, namely Cu  $K\alpha_1$ , Cu  $K\alpha_2$  and Cu  $K\beta$ . The Cu  $K\beta$  wavelength is generated by the transition of electrons from the 3p orbital, while the Cu  $K\alpha_1$  and Cu  $K\alpha_2$  wavelengths are generated by transition of electrons from the 2p orbital, differentiated due to the different spin states of electrons in the 2p subshell. The Ge monochromator removes the less intense Cu  $K\alpha_2$ , Cu  $K\beta$  and white X-rays, leaving the more intense Cu  $K\alpha_1$  radiation.

### **2.2.1.2 XRPD analysis and Rietveld Refinement**

Initial analysis was carried out by comparing powder diffraction files in the Diffrac<sup>plus</sup> EVA database to the XRPD data collected from the powder samples. Subsequently, Rietveld refinement was carried out using the GSAS suite of programmes<sup>34</sup>. It is important to note that Rietveld refinement is precisely that, a refinement technique; the starting point for determining the unit cell will come from another source. In the case of this thesis, all starting unit cell information was taken from appropriate published research found using the Inorganic Crystal Structure Database (ICSD), which contains 89,064 inorganic structures<sup>35</sup>.

Heavy metals, such as bismuth, are very good at absorbing and scattering X-rays, which leads to a change in intensity for certain peaks. Therefore, prior to Rietveld refinement it is necessary to perform an absorption correction.

Rietveld refinement is a least-squares method of calculating and refining lattice parameters, atom positions and thermal vibrations, which was developed by H.M. Rietveld in 1967<sup>32,36</sup>.

Rietveld refinement takes into account the intensity at each XRPD data point and then uses a least-squares method to estimate the structural parameters. Rietveld refinement allows for a more advanced analysis than an integration method, as it allows for impurities and overlapping peaks caused by the same phase, which would be difficult to separate through other means.

The strength of the least-squares method is that it is a method for solving overdetermined systems. For powder diffraction the equations represent powder profile points and the variables refer to parameters.

The least squares method is the minimization of the following equation:

$$M = \sum w(y_{i(obs)} - y_{i(calc)})^2$$

The variable  $w$  is the weighted mean and  $y_{i(obs)}$  and  $y_{i(calc)}$  are the observed and calculated intensities for the  $i^{\text{th}}$  point, respectively. Minimization of this equation gives parameter estimates for the set of linear equations. The minimum for the equation can be found by calculating where the first derivative of  $M$  is equal to 0, i.e.:

$$\sum w(y_{i(obs)} - y_{i(calc)})^2 \frac{\delta y_{i(calc)}}{\delta p_j} = 0$$

Where  $\delta p_j$ , represents a parameter shift. The downside of this method is that it may lead to a false minima, that is, a solution for the above equation, but not the optimal (and sometimes not even physically possible) solution for the equation.

The parameters which indicate whether a calculated pattern is a good fit to the observed pattern are  $R_p$ ,  $R_{wp}$  and  $\chi^2$ . The  $R_p$  value gives the difference between the calculated and observed pattern with no bias given to any specific point, giving a measure of how similar the two patterns are, in general. The equation used is:

$$R_p = \frac{\sum |y_i(obs) - y_i(calc)|}{\sum y_i(obs)}$$

Where  $y_i$  is the intensity for a given point  $i$ .

In a similar manner,  $R_{wp}$  gives a similar measure to  $R_p$  of the difference between the observed and calculated values. However,  $R_p$  does not take into account the standard deviation of peak heights and background radiation which makes  $R_{wp}$  a more useful measure of similarity between the two data sets. Via the following formula  $R_{wp}$  can be calculated:

$$w_i^{-1} = \sigma_i^2 = \sigma_{ip}^2 + \sigma_{ib}^2$$

Where

$\sigma_i$  = Standard deviation of the  $i$ th point

$\sigma_{ip}$  = Standard deviation of a the  $i$ th point within a peak

$\sigma_{ib}$  = Standard deviation of the  $i$ th point of the background

The calculated value of  $w_i$  is then used in a modified version of the  $R_p$  equation:

$$R_{wp} = \left[ \frac{\sum w_i (y_i(obs) - y_i(calc))^2}{\sum w_i (y_i(obs))^2} \right]^{\frac{1}{2}}$$

Where  $y_i$  is again the intensity at the  $i$ th point, and  $w_i$  is calculated as per the previous equation. Ideally, the  $R_{wp}$  value should approach the expected  $R$  value, which is a measure of the quality of the experimental data. The expected  $R$  value,  $R_{exp}$  is given by the following equation:

$$R_{exp} = \left[ \frac{N - P}{\sum_i w_i y_i(obs)^2} \right]^{\frac{1}{2}}$$

Where  $N$  is the number of points, and  $P$  is the number varied.

By taking the  $R_{wp}$  and  $R_{exp}$  values an even better measure of fit,  $\chi^2$  can be calculated, which should take the value of 1 in the case of a perfect fit between experimental and calculated data. Mathematically,  $\chi^2$  is calculated by the following equation.

$$\chi^2 = \left( \frac{R_{wp}}{R_{exp}} \right)^2$$

The GSAS programme uses a mathematical algorithm to alter unit cell and instrumental parameters to create the best theoretical fit possible between the calculated and observed data sets.

A key danger when using GSAS is that the  $\chi^2$  value can adopt a false minimum. In this situation, the  $\chi^2$  value sits in a 'well' of possible  $\chi^2$  values and needs to adopt a higher value than the false minimum to move to a superior fit. As the algorithm seeks to find the lowest  $\chi^2$  value, adopting a higher value is seen as sub-optimal, even though it is necessary in the long-term.

### **2.2.2 Physical Properties Measurement System**

Magnetic measurements were performed using a Quantum Design Model 6000 Physical Properties Measurement System (PPMS) using AC Susceptibility and DC Magnetisation (ACMS) method. Measurements were carried out, both in zero-field cooled (ZFC) and field-cooled (FC) conditions, using the DC extraction or induction method. The AC magnetic susceptometer (ACMS) uses sensing coils to measure the changes in magnetic flux that are caused by a magnetised sample.

The sample is inserted into a straw and lowered into position inside a pick-up coil. The pick-up coil is designed to detect any flux changes as the magnetised sample is moved through the coil<sup>37</sup>. The external magnetic field is applied by a niobium-titanium alloy, which acts as a superconducting magnet. The ZFC measurement is taken initially, after the sample is cooled to 3-4K, it is warmed without any external magnetic field. Once warmed, the sample is then cooled in the presence of an external field, which allows the FC measurements to be taken on warming. By calculating the magnetic susceptibility of a material, its magnetic properties can be defined.

### 2.2.3 Superconducting Quantum Interference Devices (SQUID)

To measure magnetic interactions within a material a Superconducting Quantum Interface Device (SQUID) is sometimes used. A SQUID measures magnetic fields indirectly, via a superconducting ring.

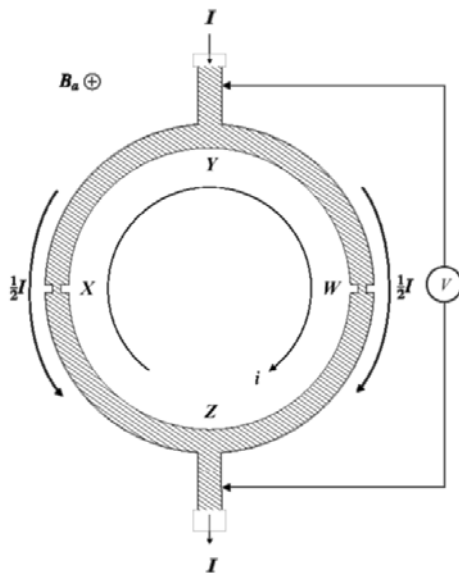


**Figure 10:** Schematic illustration of the superconducting ring of a SQUID. Edited from <http://www.cmp.liv.ac.uk/frink/thesis/thesis/img360.png> Accessed 14/08/09.

A SQUID uses the properties of Cooper pairs and Josephson tunnelling to measure magnetic fields (Figure 10). The superconducting ring contains weak links (Josephson junctions) at two opposite points. At the weak links the critical current is much lower than the rest of the ring. The lower critical current at the weak points decreases the current density, which in turn lowers the momentum of the electron pairs, so their wavelengths are long, which gives a relatively

uniform phase within the ring.

The current of superconducting materials is carried by pairs of electrons, known as Cooper pairs. Cooper pairs have wavelengths that are coherent over long distances, unlike normal conducting pairs which lose coherence due to scattering.

If two superconducting regions are separate, there is no interaction between their electron pairs. However, due to the long range coherence of Cooper pairs, if the two regions are brought in close proximity, it is possible for electron pairs to tunnel across the gap and couple the electron pair waves; this coupling effect increases as the

regions are brought closer. The tunnelling effect is known as Josephson tunnelling<sup>38</sup>.

The critical current of the gap is:

$$i_s = i_c \sin \Delta \phi \quad (a)$$

Where  $i_s$  is the supercurrent,  $i_c$  is the critical current and  $\Delta \phi$  represents the phase difference of the two regions. As the phase difference approaches  $\pi/2$ ,  $i_s$  approaches  $i_c$ .

Passing a current  $i$  through the ring produces a phase difference across the weak links. When a magnetic field, termed  $B$  is applied perpendicularly to the ring a phase difference forms between the weak points, along the paths  $XYW$  and  $WZX$ . The applied magnetic field gives a phase change equal to<sup>39</sup>:

$$\Delta \Phi(B) = 2\pi \phi_a / \phi_0 \quad (b)$$

Where  $\Phi_a$  represents the flux within the ring. The  $\Phi_0$  of this equation is a quantised unit, known as a fluxon, given by  $\Phi_0 = \frac{h}{2e} = 2.07 \times 10^{-15} \text{ Wb}$ <sup>40</sup>. Across the two weak links there is a phase change of  $2\Delta\Phi(i)$ . Therefore, the total phase difference is:

$$\Delta \Phi(B) + 2 \Delta \Phi(i) = n2\pi$$

Current energy can either be added or subtracted from the overall phase difference, but subtraction is more favourable. Using equations (a) and (b) the magnitude of the anti-clockwise current can be calculated,  $|i^-| = i_c \sin \pi (\phi_a / \phi_0)$ <sup>8</sup>.

The value for  $i$  increases to a maximum value as flux increases from 0. At the point where the flux increases over  $1/2 \Phi_0$  applying a clockwise current,  $i^+$  becomes

more favourable, upon which the flux approaches  $\Phi_0$ . The circulating current is a periodic function based on the applied field, which varies by  $\Phi_0$ . Determining the circulating current is what makes SQUID an effective magnetometer.

By using a measuring current, marked  $I$  in Figure 10, the current that circulates due to change in the flux can be detected. In a symmetrical ring, the current passes through each Josephson junction in equal proportions. When  $I$  is increased to a critical amount  $I_c$  a voltage can be measured across the ring. As the phase change across the ring will be a multiple of  $2\pi$  and the magnitude of  $I_c$  depends on the current across the weak links, the equation below must hold for a superconducting ring:

$$2\pi \frac{\Phi_a}{\Phi_0} + \alpha + \beta = n \cdot 2\pi$$

Where  $\alpha$  and  $\beta$  represent the phase changes at the weak links, while  $2\pi \Phi_a / \Phi_0$  stands for the phase change induced by the magnetic field. The sum of  $\alpha$  and  $\beta$  is constant but they are not necessarily equal, so they can be written:

$$\alpha = \pi \left[ n - \left( \frac{\Phi_a}{\Phi_0} \right) \right] - \delta \quad \text{and} \quad \beta = \pi \left[ n - \left( \frac{\Phi_a}{\Phi_0} \right) \right] + \delta$$

Where  $\delta$  is related to  $I$ , the detection current. Rearranging equation (a),  $I$  can be given as  $I = 2i_c |\cos \pi \Phi_a / \Phi_0 \cdot \sin \delta|$ . Thus, as  $\sin \delta$  has a maximum value of unity, the equation for the critical current is  $I_c = 2i_c |\cos \pi \Phi_a / \Phi_0|$  <sup>39</sup>.

This equation gives a periodic function with a maximum value of  $2i_c$  and a period of a fluxon, which depends on the strength of the magnetic field, allowing the user to calculate magnetic interactions (Figure 11).

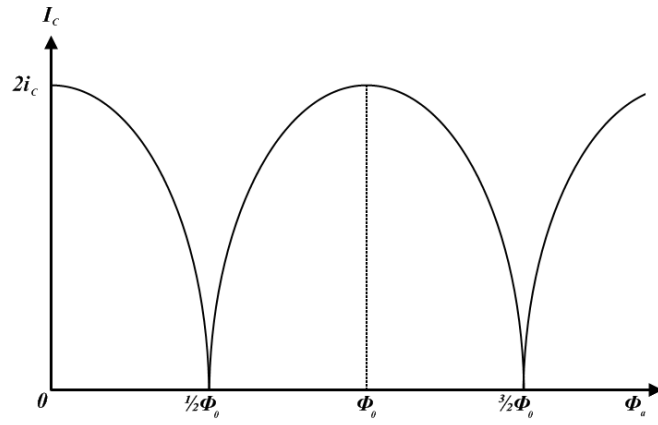


**Figure 11:** Periodic function for the critical current,  $I_c$

## **Section 3: Results and Discussion**

### **3.1 Bi<sub>3</sub>NbTiO<sub>9</sub> Characterisation**

#### **3.1.1 Bi<sub>3</sub>NbTiO<sub>9</sub>**

Tribismuth niobium titanium oxide, Bi<sub>3</sub>NbTiO<sub>9</sub>, has the two-layer Aurivillius phase structure. Analysis of the resultant material was done by XRPD, taking a scan over a 2 $\theta$  range between 5° and 100°, over a period of 12 hours. Figure 12 shows the XRPD data collected for Bi<sub>3</sub>NbTiO<sub>9</sub> and subsequently used in its characterisation.

#### **3.1.2 Characterisation of Bi<sub>3</sub>NbTiO<sub>9</sub>**

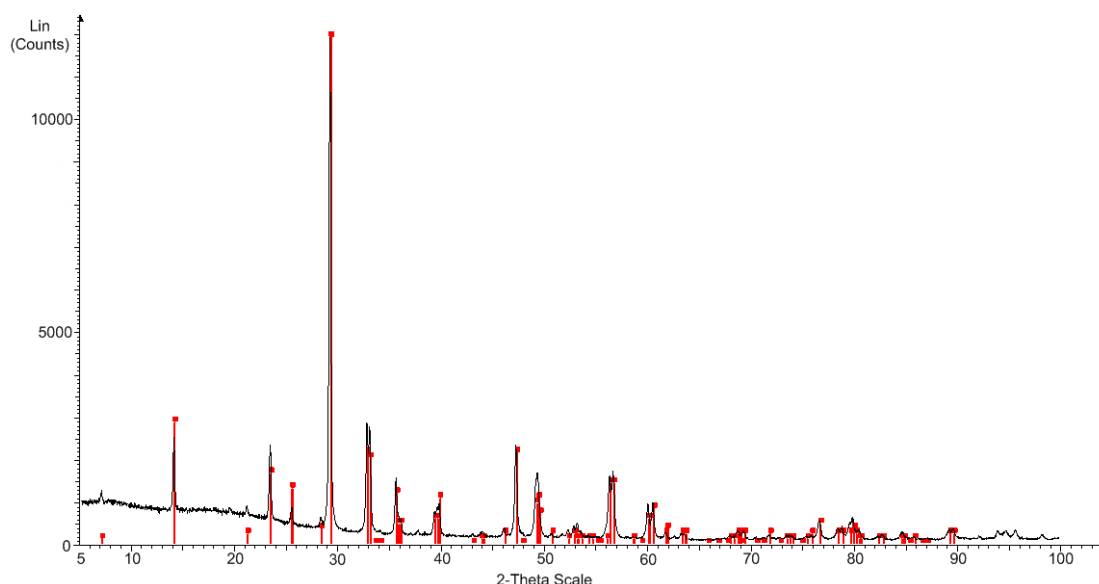


**Figure 12:** XRPD pattern of Bi<sub>3</sub>NbTiO<sub>9</sub>, with the calculated pattern for Bi<sub>3</sub>NbTiO<sub>9</sub> (72-2367).

A single phase structural refinement of the material was carried out using the programme GSAS, based on the space group  $A2_1am$ . The obtained diffraction pattern can be compared with the one calculated by GSAS.

The value of  $\chi^2=1.403$  that was calculated shows a good fit between the calculated and observed data set.  $R_{wp}$  was calculated to be 0.0562 and  $R_p$  was calculated to be 0.0337 (Figure 13). In Figure 13, and in all subsequent Rietveld

refinement profiles, the red data points represent observed data, green lines show the calculated profile, while the line underneath gives a measure of the difference between these two data sets, ideally this line is as flat as possible.

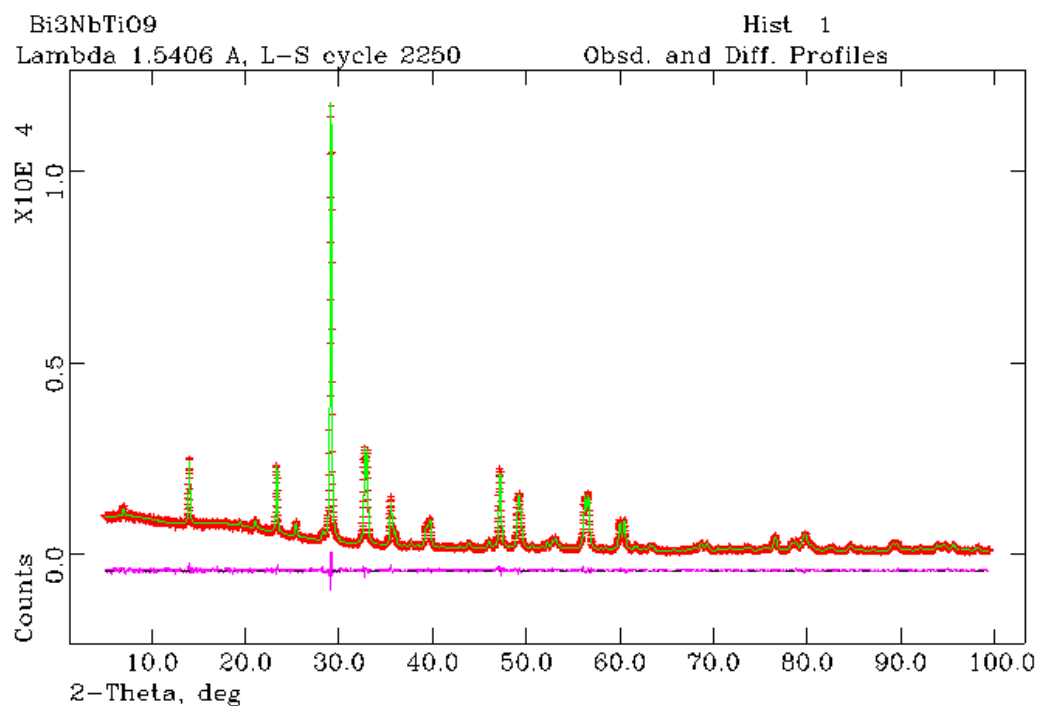


**Figure 13:** Rietveld refinement of XRPD data.

The unit cell parameters that were calculated by Rietveld refinement are  $a = 5.4564(2)\text{\AA}$ ,  $b = 5.4130(2)\text{\AA}$  and  $c = 25.1898(9)\text{\AA}$ ,  $\alpha = \beta = \gamma = 90.00^\circ$ . The positions of each atom are shown in Table 1.

Atom	Multiplicity	Fractional Coordinates			Occupancy	$U_{\text{iso}} \times 100$ ( $\text{\AA}^2$ )
		<i>x</i>	<i>y</i>	<i>z</i>		
Bi	4	0.989(2)	0.761(1)	0.500	1.0	2.4(1)
Bi	8	0.000 <sup>a</sup>	0.7327(6)	0.69908(7)	1.0	2.02(7)
Nb	8	0.042(1)	0.248(3)	0.5878(1)	0.5	0.7(2)
Ti	8	0.042(1)	0.248(3)	0.5878(1)	0.5	0.7(2)
O	4	0.078(5)	0.179(6)	0.500	1.0	0.3(4)
O	8	0.054(4)	0.289(5)	0.6641(7)	1.0	0.3(4)
O	8	0.272(8)	0.472(9)	0.246(2)	1.0	0.3(4)
O	8	0.277(9)	0.533(7)	0.569(1)	1.0	0.3(4)
O	8	0.359(4)	0.057(5)	0.584(1)	1.0	0.3(4)

**Table 1:** Unit cell data for  $\text{Bi}_3\text{NbTiO}_9$ . <sup>a</sup>Fixed to define origin of the polar axis.

The values for the unit cell obtained by Rietveld refinement correspond well to the figures on which the refinement was based. The published figures, that were used as a basis for refinement, are  $a = 5.440(7)\text{\AA}$ ,  $b = 5.394(7)\text{\AA}$  and  $c = 25.099(5)\text{\AA}$ ,

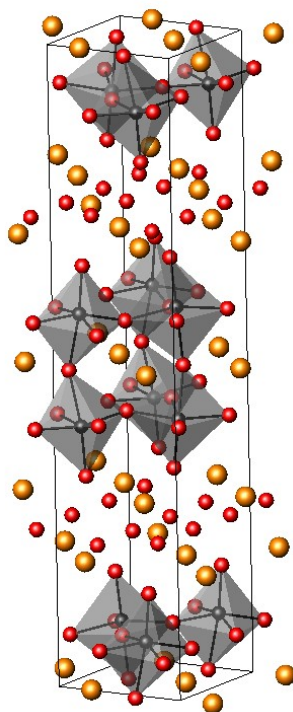


**Figure 14:** Determined structure of  $\text{Bi}_3\text{NbTiO}_9$ . The red spheres are oxygen, orange spheres are bismuth and black spheres represent niobium or titanium, ordered randomly.

$\alpha = \beta = \gamma = 90.00^\circ$ <sup>16</sup>. The data from the Rietveld refinement gives rise to the unit cell described by Figure 14.

## 3.2 Bi<sub>4</sub>Ti<sub>3</sub>O<sub>12</sub> Characterisation

### 3.2.1 Bi<sub>4</sub>Ti<sub>3</sub>O<sub>12</sub>

A three-layer Aurivillius phase material, bismuth titanate, Bi<sub>4</sub>Ti<sub>3</sub>O<sub>12</sub>, was produced using a similar methodology to the synthesis of Bi<sub>3</sub>NbTiO<sub>9</sub>. The XPRD analysis implies a single phase product Figure 15:

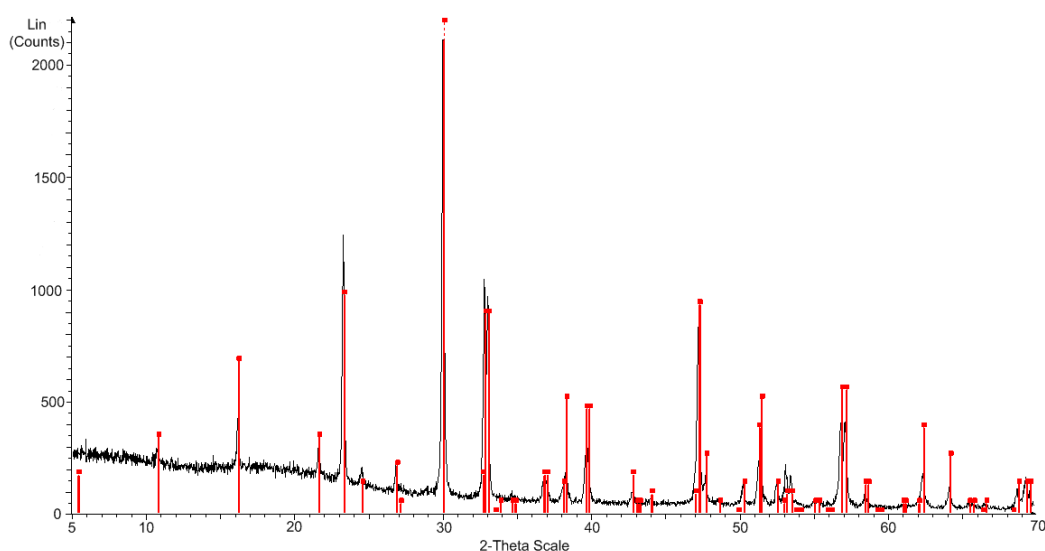


**Figure 15:** XPRD pattern of Bi<sub>4</sub>Ti<sub>3</sub>O<sub>12</sub>, the overlaid ICDD pattern is for Bi<sub>4</sub>Ti<sub>3</sub>O<sub>12</sub> (72-1019).

### 3.2.2 Characterisation of Bi<sub>4</sub>Ti<sub>3</sub>O<sub>12</sub>

Recent research papers, particularly those using single crystal data, have suggested a variety of different space groups for Bi<sub>4</sub>Ti<sub>3</sub>O<sub>12</sub>, such as *B1a1*<sup>41</sup>, *A1n1*<sup>42</sup>, and *B2cb*<sup>43</sup>. However, the space group used for the Bi<sub>4</sub>Ti<sub>3</sub>O<sub>12</sub> Rietveld refinement was based on the *Fmmm* space group, suggested by Aurivillius<sup>1</sup>. This is due to the inherent insensitivity of XRPD to oxygen positions in phases containing heavy atoms such as Bi and the lower quality of data obtained from polycrystalline samples compared with



Atom	Multiplicity	Fractional Coordinates			Occupancy	$U_{\text{iso}} \times 100$ ( $\text{\AA}^2$ )
		$x$	$y$	$z$		
Bi	8	0.000	0.000	0.06630(6)	1.0	0.57(5)
Bi	8	0.000	0.000	0.21126(6)	1.0	1.35(6)
Ti	4	0.000	0.000	0.500	1.0	3.4(4)
Ti	8	0.000	0.000	0.3709(3)	1.0	4.4(3)
O	8	0.250	0.250	0.000	1.0	6.3(3)
O	8	0.250	0.250	0.250	1.0	6.3(3)
O	8	0.000	0.000	0.4390(9)	1.0	6.3(3)
O	8	0.000	0.000	0.305(1)	1.0	6.3(3)
O	16	0.250	0.250	0.1090(7)	1.0	6.3(3)

**Table 2:** Unit cell data for  $\text{Bi}_4\text{Ti}_3\text{O}_{12}$ .

The calculated unit cell parameters are  $a = 5.4043(1)\text{\AA}$ ,  $b = 5.4432(1)\text{\AA}$  and  $c = 32.785(1)\text{\AA}$ ,  $\alpha = \beta = \gamma = 90.00^\circ$ . The values that were suggested by Aurivillius (1949) are quite similar, being  $a = 5.41\text{\AA}$ ,  $b = 5.448\text{\AA}$  and  $c = 32.84\text{\AA}$ ,  $\alpha = \beta = \gamma = 90.00^\circ$ .

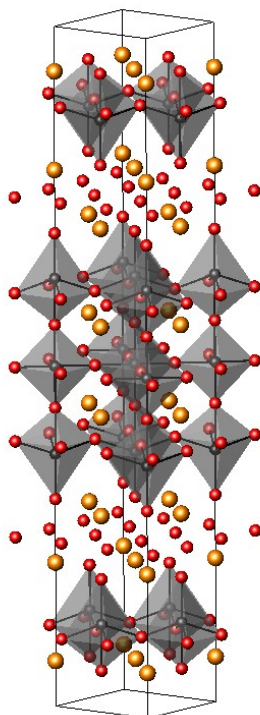


**Figure 17:** Graphical representation of the structure of  $\text{Bi}_4\text{Ti}_3\text{O}_{12}$ . The red spheres are oxygen, orange spheres are bismuth and black spheres represent titanium.

### 3.3.1 $\text{Bi}_5\text{FeTi}_3\text{O}_{15}$

The compound  $\text{Bi}_5\text{Ti}_3\text{FeO}_{15}$  is one example of a whole family of Aurivillius phase materials which are based on bismuth titanate, with iron acting as a magnetic ion with the general formula  $\text{Bi}_{x+4}\text{Fe}_x\text{Ti}_3\text{O}_{3(x+4)}$ . This four layer member of the bismuth iron titanate family (where  $x=1$ ) has a proportion of its B sites doped with Fe. The ferroelectric behaviour of  $\text{Bi}_5\text{FeTi}_3\text{O}_{15}$  has been relatively well documented<sup>47-52</sup>.

#### 3.3.1.1 Characterisation of $\text{Bi}_5\text{FeTi}_3\text{O}_{15}$

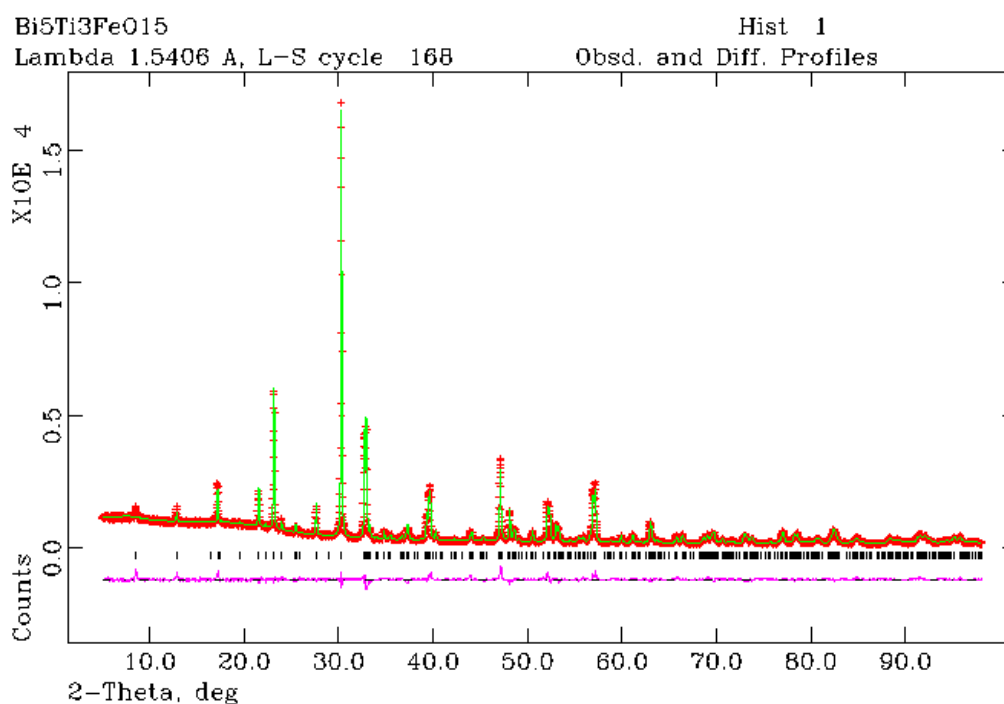


**Figure 18:** Rietveld refinement of  $\text{Bi}_5\text{FeTi}_3\text{O}_{15}$ .

X-ray powder diffraction data for  $\text{Bi}_5\text{FeTi}_3\text{O}_{15}$  was carried out over a period of 12 hours, with a  $2\theta$  range from  $5^\circ$  to  $95^\circ$ . Structural data for the Rietveld refinement of  $\text{Bi}_5\text{FeTi}_3\text{O}_{15}$  was based on structural data provided by previous work, based on the

$A2_1am$  space group<sup>53</sup>. The refinement profile had a  $\chi^2$  value of 1.224, which indicates a good fit between the observed and calculated data sets (Figure 18).

Atom	Multiplicity	Fractional Coordinates			Occupancy	$U_{\text{iso}} \times 100$ ( $\text{\AA}^2$ )
		$x$	$y$	$z$		
Bi	4	0.250 <sup>a</sup>	0.245(2)	0.000	1.0	0.63(4)
Bi	8	0.242(2)	0.246(1)	0.10463(4)	1.0	0.63(4)
Bi	8	0.228(1)	0.2696(7)	0.21909(4)	1.0	0.63(4)
Ti	8	0.2950(2)	0.247(5)	0.4513(2)	0.75	0.1(2)
Fe	8	0.2950(2)	0.247(5)	0.4513(2)	0.25	0.1(2)
Ti	8	0.293(2)	0.243(4)	0.3469(2)	0.75	0.1(2)
Fe	8	0.293(2)	0.243(4)	0.3469(2)	0.25	0.1(2)
O	4	0.315(8)	0.178(9)	0.500	1.0	0.0 <sup>b</sup>
O	8	0.601(7)	0.574(6)	0.051(1)	1.0	0.0 <sup>b</sup>
O	8	0.320(5)	0.295(8)	0.4041(6)	1.0	0.0 <sup>b</sup>
O	8	0.51(2)	0.48(1)	0.1372(9)	1.0	0.0 <sup>b</sup>
O	8	0.278(7)	0.218(9)	0.3018(6)	1.0	0.0 <sup>b</sup>
O	8	0.47(2)	0.50(3)	0.251(2)	1.0	0.0 <sup>b</sup>
O	8	0.03(1)	0.97(1)	0.0400(7)	1.0	0.0 <sup>b</sup>
O	8	0.067(8)	0.038(8)	0.147(1)	1.0	0.0 <sup>b</sup>

**Table 3:** Atom positions of  $\text{Bi}_5\text{FeTi}_3\text{O}_{15}$ , calculated by GSAS. <sup>a</sup>Fixed to define origin of the polar axis. <sup>b</sup> $U_{\text{iso}}$  fixed as Rietveld refinement tended towards negative values.

The calculated unit cell parameters are  $a = 5.4637(1)\text{\AA}$ ,  $b = 5.4342(1)\text{\AA}$  and  $c = 41.179(1)\text{\AA}$ ,  $\alpha = \beta = \gamma = 90.00^\circ$ . This compares favourably with the dimensions suggested by Hervoches *et al.* (2002), which gives  $a = 5.4698(1)\text{\AA}$ ,  $b = 5.4389(1)\text{\AA}$  and  $c = 41.197(1)\text{\AA}$ ,  $\alpha = \beta = \gamma = 90.00^\circ$ <sup>53</sup>. Figure 19 shows the structure of  $\text{Bi}_5\text{FeTi}_3\text{O}_{15}$ , as determined by Rietveld refinement.

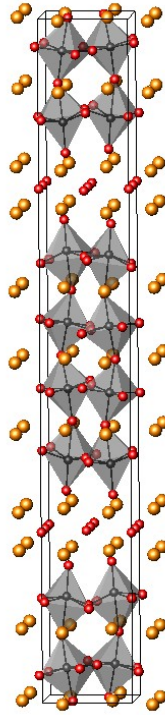


**Figure 19:** Graphical representation of the structure of  $\text{Bi}_5\text{FeTi}_3\text{O}_{15}$ . The red spheres are oxygen, orange spheres are bismuth and black spheres represent titanium.

The  $\text{Bi}_5\text{FeTi}_3\text{O}_{15}$  sample was placed into the PPMS and cooled to 4K and a field of 1000Oe was applied, before the sample was allowed to heat up to room temperature. By plotting the magnetic dipole moment in electromagnetic units against temperature in Kelvin (Figure 20) it can be seen that the magnetic dipole moment increases as temperature decreases, which is clearly a sign of paramagnetic behaviour. By plotting  $\chi$  against temperature in Kelvin, a plot is obtained that can be interpreted by using the Curie-Weiss law. The Curie-Weiss law:

$$\chi = \frac{C}{T - \theta}$$

To more accurately calculate the magnetic properties it is necessary to add a constant to represent temperature independent properties, such as the inherent diamagnetism of paired electrons. Adding a constant to the Curie-Weiss law gives:

$$\chi = \frac{C}{T - \theta} + \chi_0$$

Where  $\chi$  is the magnetic susceptibility, T is the temperature (in K) and  $\theta$  represents the critical temperature. The constants C and  $\chi_0$  represent the material-specific Curie constant and the temperature independent magnetic characteristics, respectively. The calculated variables tell us several things about the magnetic properties of  $\text{Bi}_5\text{FeTi}_3\text{O}_{15}$ . A positive  $\theta$  indicates that the predominant interactions are ferromagnetic even though magnetic ordering may not occur. A negative  $\theta$  implies predominantly anti-ferromagnetic interactions.

The fitted curve (the red line in Figure 20) for  $\chi$  plotted against T, has a  $R^2$  value of 0.99982, which indicates a high goodness of fit. The equation of the fitted curve gives a  $\theta$  value of -5.282K, indicative of latent anti-ferromagnetic character. With a

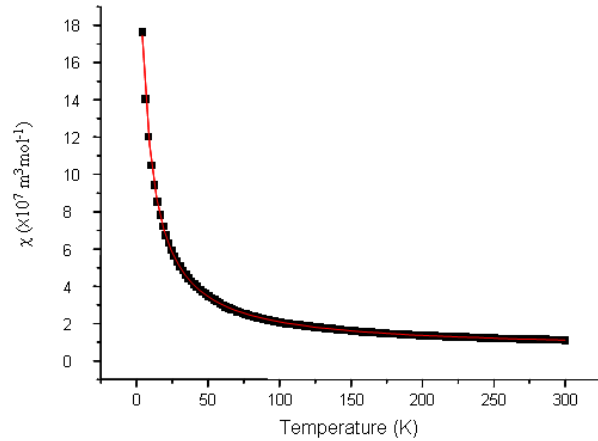


**Figure 20:** Graph showing the relationship between magnetic susceptibility and temperature for  $\text{Bi}_5\text{FeTi}_3\text{O}_{15}$ .

value of C determined to be  $1.573 \times 10^{-5}$ , the paramagnetic moment has been calculated to be  $3.164 \mu_B$ . This is lower than the calculated and experimental values for the magnetic moment of  $\text{Fe}^{3+}$ ,  $5.92 \mu_B$  and  $5.9 \mu_B$ <sup>54</sup>, respectively. This would appear to indicate that the Fe cations adopt an intermediate spin-state<sup>55</sup>, which has also been suggested in other iron-substituted Aurivillius phase materials, such as  $\text{Bi}_2\text{Sr}_2\text{Nb}_{2.5}\text{Fe}_{0.5}\text{O}_{12}$ <sup>56</sup>.

### 3.3.2 Alternative Synthesis of $\text{Bi}_5\text{FeTi}_3\text{O}_{15}$

An alternative synthesis of  $\text{Bi}_5\text{FeTi}_3\text{O}_{15}$  to the one in the table was attempted, using a different methodology. First by making  $\text{Bi}_4\text{Ti}_3\text{O}_{12}$ , and then adding stoichiometric amounts of  $\text{Bi}_2\text{O}_3$  and  $\text{Fe}_2\text{O}_3$ , before reheating. The  $\text{Bi}_4\text{Ti}_3\text{O}_{12}$  was produced by mixing stoichiometric amounts of  $\text{Bi}_2\text{O}_3$  and  $\text{TiO}_2$  and then heating to  $800^\circ\text{C}$  for 24 hours (Figure 21).

After the  $\text{Bi}_2\text{O}_3$  and  $\text{Fe}_2\text{O}_3$  were added, the subsequent mixture was heated for 8 hours at  $900^\circ\text{C}$ . Only

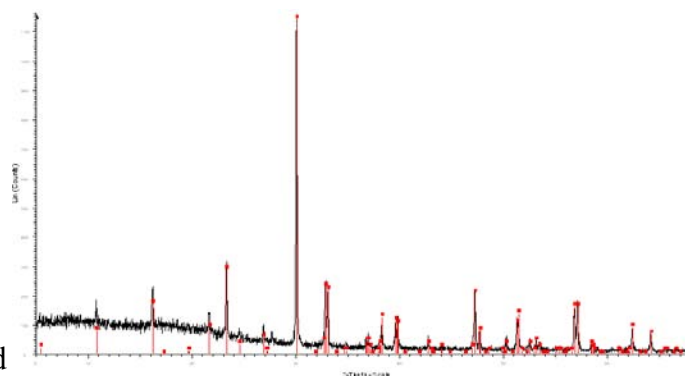


**Figure 21:** Scan pattern of  $\text{Bi}_4\text{Ti}_3\text{O}_{12}$  compared to the file pattern of  $\text{Bi}_4\text{Ti}_3\text{O}_{12}$  in red. The card number for  $\text{Bi}_4\text{Ti}_3\text{O}_{12}$  is 72-1019.

$\text{Bi}_5\text{FeTi}_3\text{O}_{15}$  was produced by both synthesis methods. The resulting material was compared to the other sample of  $\text{Bi}_5\text{FeTi}_3\text{O}_{15}$  produced by the single-firing method (Figure 22).

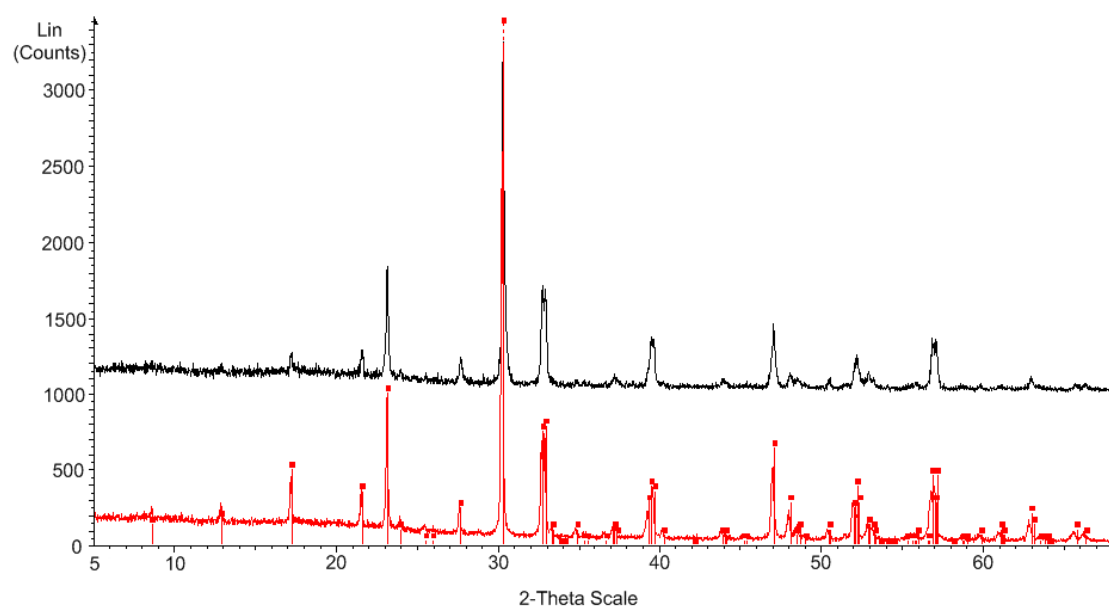


**Figure 22:** Comparison of the two samples of  $\text{Bi}_5\text{FeTi}_3\text{O}_{15}$ . The black line is the method producing  $\text{Bi}_5\text{FeTi}_3\text{O}_{15}$  via  $\text{Bi}_4\text{Ti}_3\text{O}_{12}$ , while the red line represents the single-fired sample. The ICDD card data for  $\text{Bi}_5\text{FeTi}_3\text{O}_{15}$  is overlaid (82-0063).

In this work, a variety of Aurivillius phases were formed, with the general formula  $\text{Bi}_5\text{Fe}_{x+1}\text{Ti}_{3-x}\text{O}_{15}$ . These Aurivillius phase materials all have four layers and samples were synthesised with different values of  $x$ . The value for  $x$  increased in increments of 0.1, starting at  $x=0.1$ , to create  $\text{Bi}_5\text{Fe}_{1.1}\text{Ti}_{2.9}\text{O}_{15}$  and ending at  $x=1$ ,  $\text{Bi}_5\text{Fe}_2\text{Ti}_2\text{O}_{15}$ .

### 3.3.3.1 Characterisations of $\text{Bi}_5\text{Fe}_{x+1}\text{Ti}_{3-x}\text{O}_{15}$

All of the  $\text{Bi}_5\text{Fe}_{x+1}\text{Ti}_{3-x}\text{O}_{15}$  variants underwent XRPD analysis for 6 hours each with a  $2\theta$  range from  $10^\circ$  to  $70^\circ$ , which showed the similarity between the varying compositions, and is clearly visible in Figure 23:

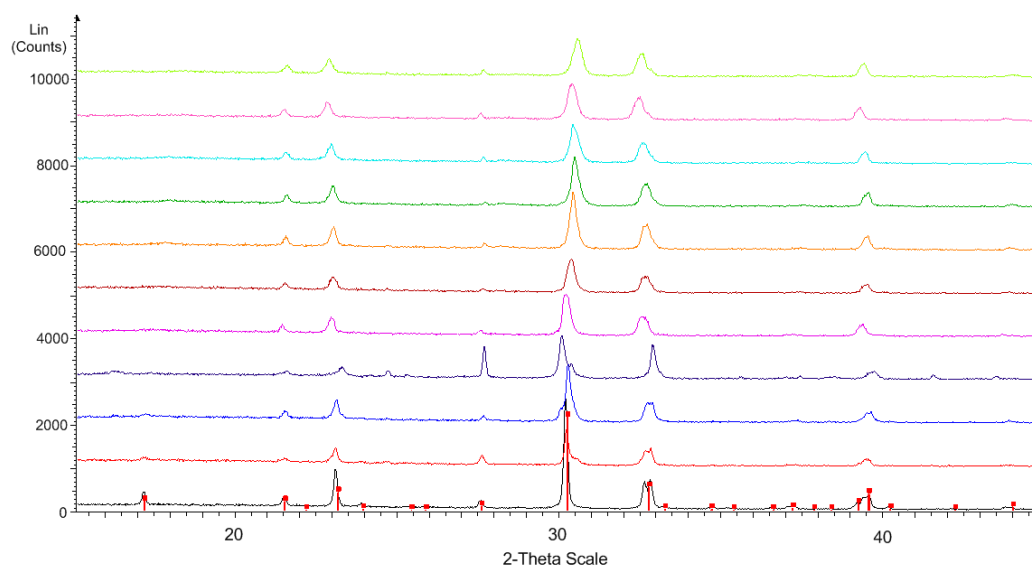


**Figure 23:** XRPD scan patterns of  $\text{Bi}_5\text{Fe}_{1+x}\text{Ti}_{3-x}\text{O}_{15}$ . From top to bottom,  $\text{Bi}_5\text{Fe}_2\text{Ti}_2\text{O}_{15}$ ,  $\text{Bi}_5\text{Fe}_{1.9}\text{Ti}_{2.1}\text{O}_{15}$ ,  $\text{Bi}_5\text{Fe}_{1.8}\text{Ti}_{2.2}\text{O}_{15}$ ,  $\text{Bi}_5\text{Fe}_{1.7}\text{Ti}_{2.3}\text{O}_{15}$ ,  $\text{Bi}_5\text{Fe}_{1.6}\text{Ti}_{2.4}\text{O}_{15}$ ,  $\text{Bi}_5\text{Fe}_{1.5}\text{Ti}_{2.5}\text{O}_{15}$ ,  $\text{Bi}_5\text{Fe}_{1.4}\text{Ti}_{2.6}\text{O}_{15}$ ,  $\text{Bi}_5\text{Fe}_{1.3}\text{Ti}_{2.7}\text{O}_{15}$ ,  $\text{Bi}_5\text{Fe}_{1.2}\text{Ti}_{2.8}\text{O}_{15}$ ,  $\text{Bi}_5\text{Fe}_{1.1}\text{Ti}_{2.9}\text{O}_{15}$  and  $\text{Bi}_5\text{FeTi}_3\text{O}_{15}$ . The ICDD card data for  $\text{Bi}_5\text{FeTi}_3\text{O}_{15}$  (38-1257) is overlaid along the bottom.

In addition, compositions  $x = 0$ ,  $x = 0.5$  and  $x = 1.0$  all underwent Rietveld refinement to investigate the unit cell structures of these compounds. The  $\text{Bi}_5\text{FeTi}_3\text{O}_{15}$  could be compared to existing published data on this compound, whereas the

refinement of the  $\text{Bi}_5\text{Fe}_{1.5}\text{Ti}_{2.5}\text{O}_{15}$  and  $\text{Bi}_5\text{Fe}_2\text{Ti}_2\text{O}_{15}$  compositions provided new data on these previously unreported compounds, opening up new lines of inquiry.

### 3.3.3.2 Characterisation of $\text{Bi}_5\text{Fe}_{1.5}\text{Ti}_{2.5}\text{O}_{15}$

Rietveld refinement carried out on the  $\text{Bi}_5\text{Fe}_{1.5}\text{Ti}_{2.5}\text{O}_{15}$  provided results that were inconclusive. The best result achieved was for the space group  $Fmm2$ , and had a  $\chi^2$  value of 5.424. While this  $\chi^2$  value is relatively low, you can see from the difference line in Figure 24 that several peaks are not fitted. In addition, a large number of peaks are lacking in intensity or the fine detail observed in the XRPD pattern (Figure 24).

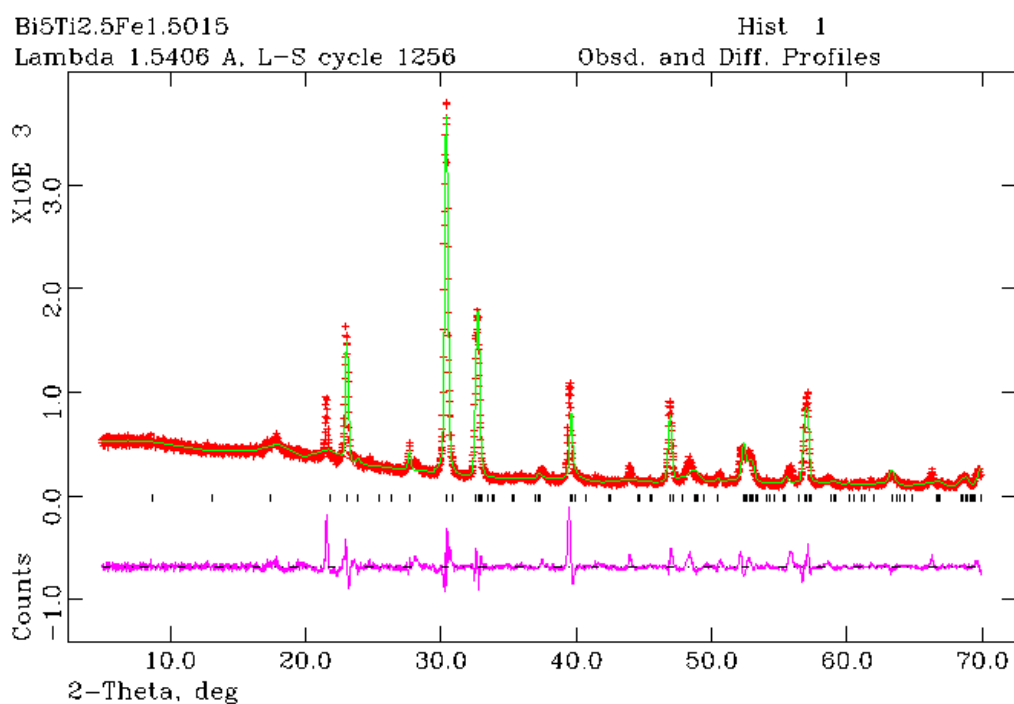


**Figure 24:** Rietveld refinement of  $\text{Bi}_5\text{Fe}_{1.5}\text{Ti}_{2.5}\text{O}_{15}$

### 3.3.4 Synthesis of $\text{Bi}_5\text{Fe}_{2+x}\text{Ti}_{2-x}\text{O}_{15}$

After the substitution of half of the B-cation sites with  $\text{Fe}^{3+}$  in  $\text{Bi}_5\text{Fe}_2\text{Ti}_2\text{O}_{15}$ , the next progression would be to increase the degree of substitution. This was to find more detail about the structural changes that occur as the iron content is increased. The new materials produced had the formula  $\text{Bi}_5\text{Fe}_{2.5}\text{Ti}_{1.5}\text{O}_{15}$  and  $\text{Bi}_5\text{Fe}_3\text{TiO}_{15}$ , increasing the iron content in the B-site to 62.5% and 75%, respectively.

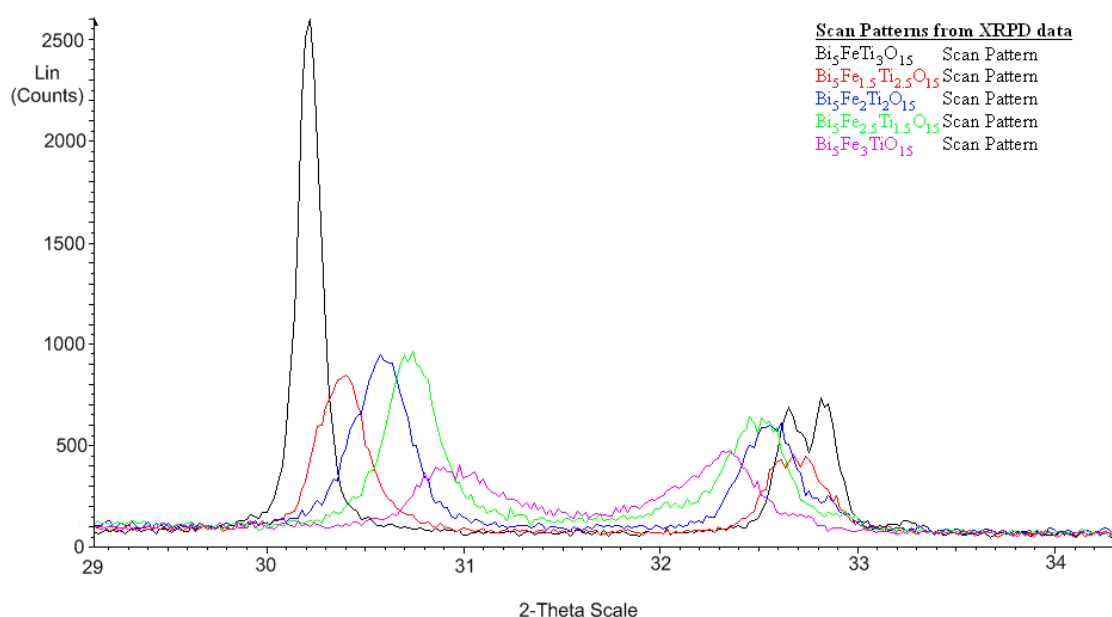


**Figure 25:** Example of peak shifting as Fe content increases in  $\text{Bi}_5\text{Fe}_{1+x}\text{Ti}_{3-x}\text{O}_{15}$ . Another example can be seen in Appendix A, Figure 1.

The new samples were processed in a manner similar to previous methods, where stoichiometric amounts of  $\text{Bi}_2\text{O}_3$ ,  $\text{Fe}_2\text{O}_3$  and  $\text{TiO}_2$  were ground together, before being fired in a furnace. Increasing the proportion of  $\text{Fe}^{4+}$  exacerbated the peak shifts seen previously (Figure 25). This shows that increasing the  $\text{Fe}^{4+}$  content has an effect on the size of the unit cell, due to the difference in size between the two ionic radii. According to the tolerance factor arguments in Section 1.3, the ionic radius of  $\text{Fe}^{4+}$  (0.585Å) falls within the calculated acceptable range of 0.58-0.65Å. However,

without the acquisition of further data, the exact effects of increasing the iron content are unknown, including the possibility of oxygen deficiencies occurring, which would give a possible non-stoichiometric formula of  $\text{Bi}_5\text{Fe}_3\text{TiO}_{15-\delta}$ .

### 3.3.4.1 Magnetic Characterisation of $\text{Bi}_5\text{Fe}_2\text{Ti}_2\text{O}_{15}$ and $\text{Bi}_5\text{Fe}_3\text{TiO}_{15}$

Samples of  $\text{Bi}_5\text{Fe}_2\text{Ti}_2\text{O}_{15}$  and  $\text{Bi}_5\text{Fe}_3\text{TiO}_{15}$  were subjected to analysis by Superconducting Quantum Interference Device (SQUID), to assess their magnetic character. The samples were both cooled from a temperature of 300K down to 5K. The samples were then heated from 5K up to 300K, first in a field of 100Oe, and then underwent this process again, but this time without the application of an external magnetic field.

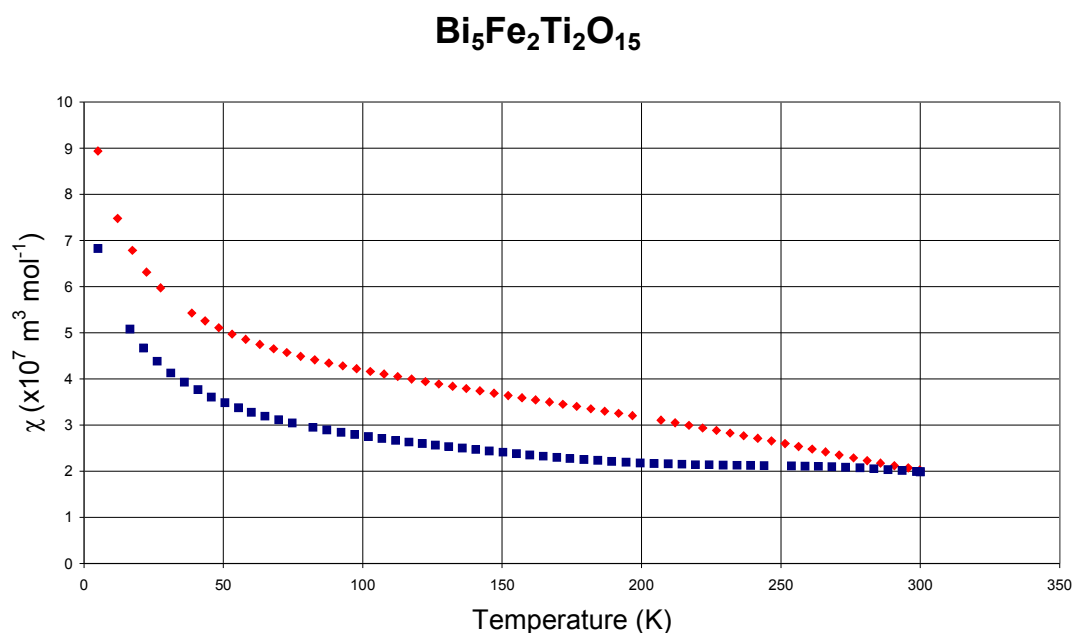


**Figure 26:** Graph showing the relationship between  $\chi$  and temperature for  $\text{Bi}_5\text{Fe}_2\text{Ti}_2\text{O}_{15}$ . Zero-field cooled (ZFC) data is in blue, while field cooled (FC) data is in red.

The plot of  $\chi$  against temperature for  $\text{Bi}_5\text{Fe}_2\text{Ti}_2\text{O}_{15}$  (Figure 26) shows paramagnetism, as the value of  $\chi$  decays almost exponentially as temperature

increases. However, the FC data retains a gradient, whereas the ZFC data reaches a plateau.

By plotting  $1/\chi$  against T (Figure 27), the constants C and  $\theta$  can be calculated. The field cooled data gives a C value of  $9.221 \times 10^{-5}$  and a  $\theta$  value of 114.74. The zero field cooled data gives a C value of  $1.036 \times 10^{-4}$  and a  $\theta$  value of 253.42. The field cooled data is fitted better, with an  $R^2$  value of 0.957915 compared to the  $R^2$  value of 0.901632 for the zero field cooled data.

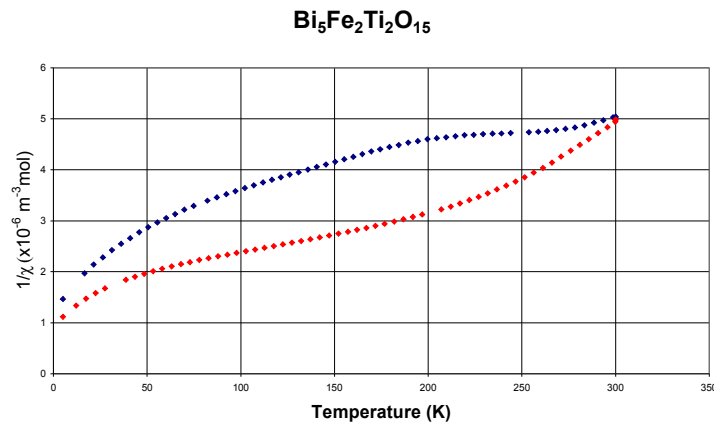


**Figure 27:** Graph showing the relationship between  $1/\chi$  and temperature for  $\text{Bi}_5\text{Fe}_2\text{Ti}_2\text{O}_{15}$ . Zero-field cooled (ZFC) data is in blue, while field cooled (FC) data is in red.

The FC measurements for  $\text{Bi}_5\text{Fe}_3\text{TiO}_{15}$  (Figure 28) need to be repeated as a machine error stopped measurements being taken above 36K. Repeating FC measurements would provide more information about the magnetic characteristics of the material, as it is difficult to get a good fit of the data, considering the slope of the ZFC data.

The ZFC curve appears to show anti-ferromagnetism, with a reduction of  $\chi$  as temperature decreases. If this is indeed an antiferromagnet, it would have a Neel temperature ( $T_N$ )  $\geq 300\text{K}$ . However, for accurate determination of the magnetic

properties of both  $\text{Bi}_5\text{Fe}_2\text{Ti}_2\text{O}_{15}$  and  $\text{Bi}_5\text{Fe}_3\text{TiO}_{15}$ , data are required for temperatures above 300K.

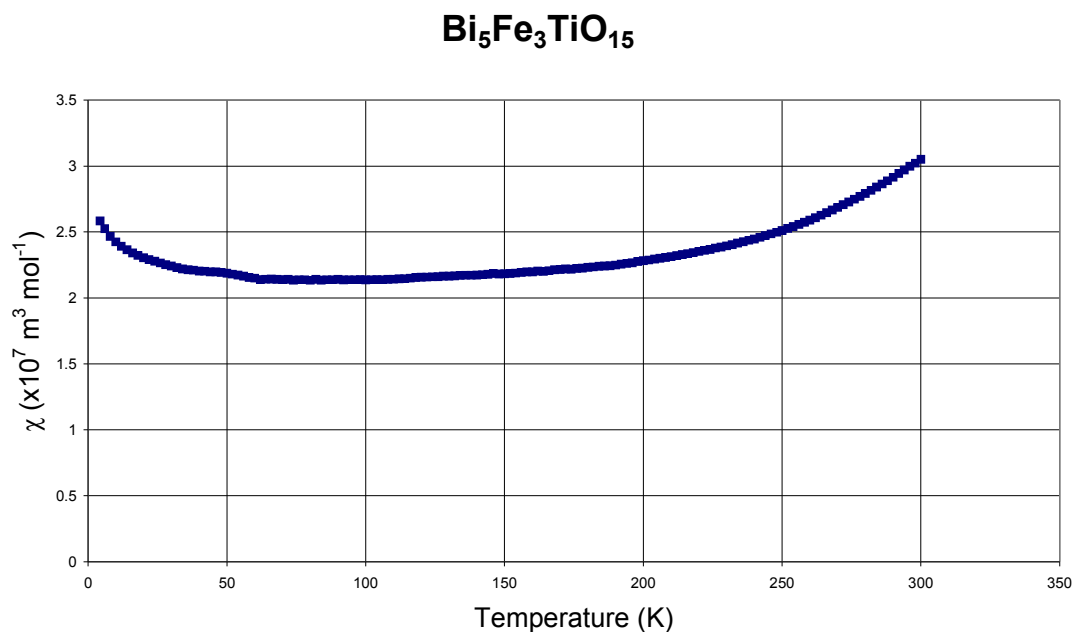


**Figure 28:** Graph showing the relationship between  $\chi$  and temperature for  $\text{Bi}_5\text{Fe}_3\text{TiO}_{15}$ . The blue line represents zero-field cooled (ZFC) data. Note that the FC data stopped at  $\sim 36\text{K}$  due to machine error, so has not been included on this graph.

### 3.3.5 Attempted Synthesis of $\text{Bi}_5\text{Fe}_4\text{O}_{15}$

After producing  $\text{Bi}_5\text{Fe}_3\text{TiO}_{15}$ , the next step was to increase the iron content to full substitution, replacing all the B-cation sites in the 4-layer Aurivillius phase with iron. A stoichiometric ratio of  $\text{Bi}_2\text{O}_3$  and  $\text{Fe}_2\text{O}_3$  was ground together with a mortar and pestle. The mixture was pre-sintered for 3 hours at  $400^\circ\text{C}$  and then was placed in a tube furnace and heated to  $800^\circ\text{C}$  for 24 hours.

The resulting mixture was removed from the furnace and ground, before undergoing XRPD analysis. The resulting XRPD pattern indicated the presence of a mixture of  $\text{BiFeO}_3$  and  $\text{Bi}_{12}(\text{Bi}_{0.5}\text{Fe}_{0.5})\text{O}_{19.5}$ , rather than a new Aurivillius phase material (Figure 29).

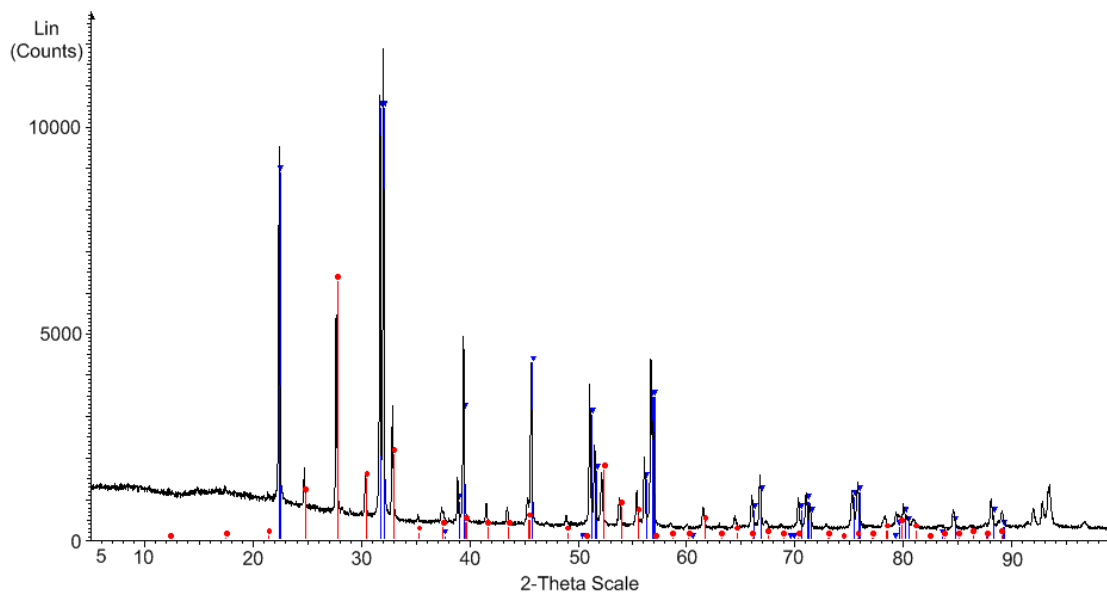


**Figure 29:** XRPD pattern of attempted  $\text{Bi}_5\text{Fe}_4\text{O}_{15}$  sample, the vertical blue lines show the patterns on file for  $\text{BiFeO}_3$  (71-2494) and the red lines are associated with  $\text{Bi}_{12}(\text{Bi}_{0.5}\text{Fe}_{0.5})\text{O}_{19.5}$  (77-0568).

### 3.4 Attempted Syntheses of $\text{Bi}_5\text{Mn}_{1+x}\text{Ti}_{3-x}\text{O}_{15}$

The formation of another 4-layer Aurivillius phase with the same structure as  $\text{Bi}_5\text{Fe}_{y+1}\text{Ti}_{3-y}\text{O}_{15}$ , except with  $\text{Mn}^{3+/4+}$  ions instead of  $\text{Fe}^{3+/4+}$  ions,  $\text{Bi}_5\text{Mn}_{x+1}\text{Ti}_{3-x}\text{O}_{15}$  was attempted. Again, the value of  $x$  was varied between 0 and 1, again increasing by intervals of 0.1, in an attempt to produce samples ranging from  $\text{Bi}_5\text{MnTi}_3\text{O}_{15}$  to  $\text{Bi}_5\text{Mn}_2\text{Ti}_2\text{O}_{15}$ . The Mn-doped samples were fired in similar conditions to the Fe-doped samples. Reaction conditions were similar to those of  $\text{Bi}_5\text{Fe}_{1+x}\text{Ti}_{3-x}\text{O}_{15}$ , as outlined by previous studies<sup>50,57</sup>.

Samples were fired at  $850^\circ\text{C}$  for 8 hours in oxygen under atmospheric pressure. The samples were then ground for 15 minutes. The samples were subsequently fired at  $900^\circ\text{C}$  for 6 hours, again in oxygen under atmospheric pressure. The samples were then ground and before the treatment at  $900^\circ\text{C}$  was then repeated.

The samples were analysed using XRPD. The diffraction pattern obtained looked to correspond more closely to a variety of compounds rather than the desired  $\text{Bi}_5\text{Mn}_{1+x}\text{Ti}_{3-x}\text{O}_{15}$ . The Bruker AXS Diffrac<sup>plus</sup> EVA database did not contain a powder diffraction file for any any value of  $x$  for  $\text{Bi}_5\text{Mn}_{1+x}\text{Ti}_{3-x}\text{O}_{15}$ , and did not closely match the  $\text{Fe}^{3+}$  analogue,  $\text{Bi}_5\text{FeTi}_3\text{O}_{15}$  (Figure 30).

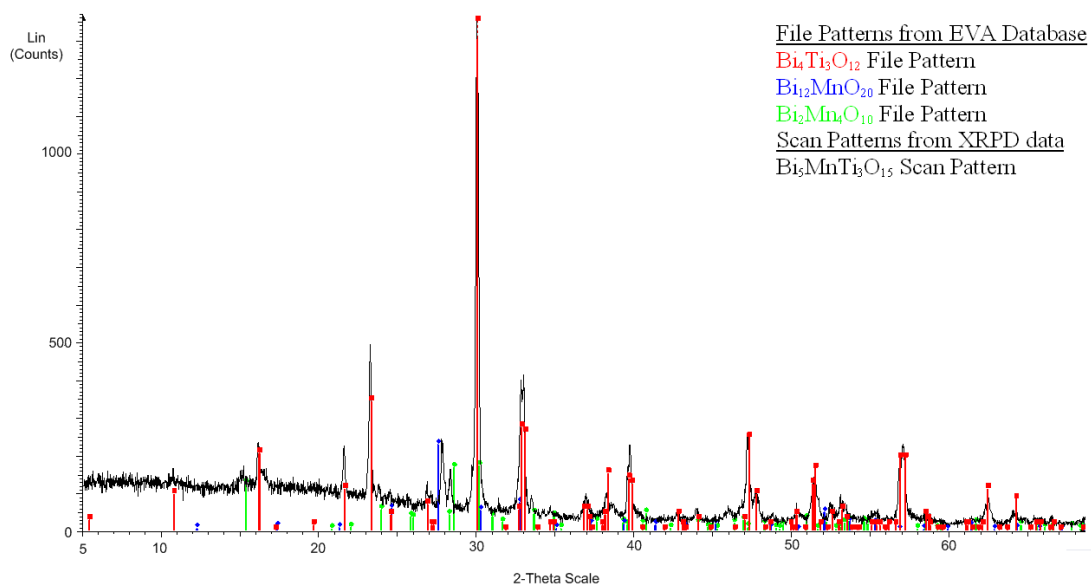


**Figure 30:** XRPD pattern of attempted  $\text{Bi}_5\text{MnTi}_3\text{O}_{15}$  with the patterns of compounds suspected to comprise the sample. The PDF2 numbers from the ICDD are:  $\text{Bi}_4\text{Ti}_3\text{O}_{12}$  – 73-2181,  $\text{Bi}_{12}\text{MnO}_{20}$  – 82-1024 and  $\text{Bi}_2\text{Mn}_4\text{O}_{10}$  – 74-1096.

Instead of continuing with the previous methodology, the problem was approached from another angle, using  $\text{MnO}_2$ , instead of  $\text{Mn}_2\text{O}_3$ . The samples were fired at increasing temperatures, 600°C, 800°C and 950°C for two hours each with intermittent grinding. The resultant material was then fired twice for 4 hours at 1000°C. To create the appropriate oxidation state for the manganese the reaction condition of the last firing relied on 10% hydrogen, 90% nitrogen gas at atmospheric pressure, to create a reducing atmosphere.

The diffraction pattern obtained for both samples of  $\text{Bi}_5\text{MnTi}_3\text{O}_{15}$ , resembled a mixture of  $\text{Bi}_2\text{Mn}_4\text{O}_{10}$ ,  $\text{Bi}_{12}\text{MnO}_{20}$  and  $\text{Bi}_4\text{Ti}_3\text{O}_{12}$  rather than

$\text{Bi}_5\text{MnTi}_3\text{O}_{15}$ , using diffraction data from the EVA database. Diffraction patterns for  $\text{Bi}_5\text{Mn}_{1+x}\text{Ti}_{3-x}\text{O}_{15}$  are included in Appendix A.

While  $\text{Mn}^{3+}$  appears to fulfil the criteria for successful (and significant) B-site substitution, the methodology outlined would appear to be unsuccessful. Although manganese cation substitution into Aurivillius phase structures is technically possible (as in the radius and charge of  $\text{Mn}^{3+}$  would make it a suitable cation for the position), without further verification of these papers by another source, it would suggest that the most prudent course of action would be to remain incredibly sceptical of the findings of these papers.

Several papers advise the use of a modest excess of  $\text{Bi}_2\text{O}_3$  to offset the losses of  $\text{Bi}_2\text{O}_3$ . Also, as  $\text{Bi}_2\text{O}_3$  has a melting point of approximately  $825^\circ\text{C}$ , the excess molten  $\text{Bi}_2\text{O}_3$  can allow the reaction to be self-fluxed. Considering the reaction conditions, extra  $\text{Bi}_2\text{O}_3$  can reliably form a range of compounds with  $\text{TiO}_2$  and  $\text{Mn}_2\text{O}_3$ , including a 3-layer Aurivillius phase,  $\text{Bi}_4\text{Ti}_3\text{O}_{12}$ , which would make the characterisation of any collected data more difficult.

## **Section 4: Conclusions and Further Work**

### **4.1 Conclusions**

The production and synthesis of both  $\text{Bi}_3\text{TiNbO}_9$  and  $\text{Bi}_4\text{Ti}_3\text{O}_{12}$  is a relatively routine procedure, when using the ceramic method. Substitution of  $\text{Fe}^{3+/4+}$  into the four layer Aurivillius phase structure is possible to levels beyond those previously reported. However, the modifications to the structure that occur are possibly outside those that are calculable by GSAS refinement of powder data.

There are multiple possibilities for the change between the  $\text{Bi}_5\text{Fe}_{1+x}\text{Ti}_{3-x}\text{O}_{15}$  phases as the Fe:Ti proportion increases. To determine how the change in structure takes place will require more data and possibly the use of additional techniques, as outlined in the section entitled 'Further Work'.

The inability to produce  $\text{Bi}_5\text{Mn}_{1+x}\text{Ti}_{3-x}\text{O}_{15}$  raises doubts about previous papers<sup>50,57</sup>. Based on the data collected as part of this project it is unlikely to be possible using the methodologies outlined. The papers in question certainly require a greater degree of scrutiny to ascertain the veracity of their conclusions.

However, the possibility to achieve significant manganese substitution should not be overlooked because of this. The techniques used may require more severe reaction conditions, or possibly co-substitution with another cation, in either the A or B sites as manganese ions typically prefer a higher oxidation state than  $\text{Mn}^{3+}$ .

It is therefore clear that bismuth layer structure ferroics contain a great deal of potential. Their flexibility and versatility should not be overlooked when designing

materials for various applications. In the future, it may be possible to tailor Aurivillius phase structure materials for specific uses.

## **4.2 Further Work**

Further work should focus on obtaining more information about the structure of the  $\text{Bi}_5\text{Fe}_{1+x}\text{Ti}_{3-x}\text{O}_{15}$  phases where  $x$  is greater than 0. While the unit cell structure of the  $\text{Bi}_5\text{FeTi}_3\text{O}_{15}$  phase is relatively well-documented the new phases derived from this material may have diverged in a variety of ways.

Single crystal X-ray diffraction or neutron diffraction may be necessary to eliminate various permutations of the unit cell, for instance the tilting and twisting of the  $(\text{Ti}, \text{B})\text{O}_6$  can make accurate determination of the unit cells of various Aurivillius phases more difficult. A degree of structural degeneracy could account for the difficulty in refining the unit cells.

Another possibility would be that the materials with increased iron content create an intergrowth phase, containing an increasing proportion of  $\text{BiFeO}_3$  sub-layers. In this instance electron microscopy techniques, such as Scanning Electron Microscopy (SEM), or Transmission Electron Microscopy (TEM) may be necessary to determine the layer structure of the newly-created phases. Electron microscopy has been used for this purpose, to great effect, in observing the layering in materials such as  $\text{Bi}_7\text{Ti}_4\text{NbO}_{21}$ <sup>58</sup>.

After submission, Mössbauer spectroscopy is due to be carried out on the  $\text{Bi}_5\text{FeTi}_3\text{O}_{15}$ ,  $\text{Bi}_5\text{Fe}_2\text{Ti}_2\text{O}_{15}$ ,  $\text{Bi}_5\text{Fe}_3\text{TiO}_{15}$  and  $\text{Bi}_5\text{Fe}_4\text{O}_{15}$  samples. Appendix B contains information on the Mössbauer spectroscopy technique. The primary information that is obtainable from Mössbauer spectroscopy is the oxidation state of the Fe cations.

Additionally, information about whether or not electron exchange is occurring and magnetic interactions can be collected, amongst other details.

Further work should also consider the substitutions of other magnetic ions and also possibilities involving co-substitution. The substitution for other ions in the place of  $\text{Bi}^{3+}$  should also be attempted to alter the properties of Aurivillius phase materials. Additional lines of enquiry would include increasing the number of layers within the Aurivillius phase structure and using intergrowth behaviours to modify the properties of materials.

As well as cations, the anion sites of bismuth layer structure can have the oxygen replaced by other anions, as witnessed in  $\text{Bi}_2\text{TiO}_4\text{F}_2$  and  $\text{Bi}_2\text{NbO}_5\text{F}^{59}$ . This provides another option in altering the properties of the layered structure. In conclusion, the versatility of Aurivillius phase materials provides a wealth of potential and opportunity for any chemist.

- <sup>1</sup>B. Aurivillius, (1949), *Arkiv for Kemi*, Volume 1, Iss. 6, p499-512
- <sup>2</sup>K. Aizu, (1969), *Journal of the Physical Society of Japan*, Vol. 27, p387
- <sup>3</sup>S.C. Abrahams, (1971), *Materials Research Bulletin*, Vol. 6, p881-890
- <sup>4</sup>N.A. Hill, A. Filippetti, (2002), *Journal of Magnetism and Magnetic Materials*, Volume 242, p976
- <sup>5</sup>H. Schmid, (1994), *Bulletin of Material Sciences*, Volume 17, Iss. 7, p1411
- <sup>6</sup>H. Schmid, (1973), *International Journal of Magnetism*, Volume 4, p337
- <sup>7</sup>E. Ascher, (1973), *International Journal of Magnetism*, Volume 5, p287
- <sup>8</sup>R.R. Birss, (1963), *Report on Progress in Physics*, Vol. 26, p307
- <sup>9</sup>K. Aizu, (1970), *Physical Review B*, Volume 2, Num. 3, p754
- <sup>10</sup>C.A. De Araujo, J.D. Cuchiaro, L.D. McMillan, M.C. Scott, J.F. Scott, (1995), *Nature*, Volume 374, p627
- <sup>11</sup>B. Aurivillius, (1950), *Arkiv for Kemi*, Volume 2, Iss. 6, p519-527
- <sup>12</sup>A.M. Kusainova, P. Lightfoot, W. Zhou, S.Y. Stefanovich, A.V. Mosunov and V.A. Dolgikh, (2001), *Chemistry of Materials*, Volume 13, p4731
- <sup>13</sup>G.A. Smolenskii, V.A. Isupov, A.I. Agranovskaya, (1959), *Soviet Physics Solid-State*, Volume 1, Iss. 1, p149
- <sup>14</sup>E.C. Subbarao, (1961), *Journal of Physics and Chemistry of Solids*, Volume 23, June Iss., p665
- <sup>15</sup>R.E. Newnham, R.W. Wolfe, J.F. Dorrian, (1971), *Materials Research Bulletin*, Volume 6, p1029-1046
- <sup>16</sup>J.G. Thompson, A.D. Rae, R.L. Withers and D.C. Craig, (1990), *Acta Crystallographica*, Volume B47, p174
- <sup>17</sup>J.G. Thompson, R.L. Withers and A.D. Rae, (1991), *Journal of Solid State Chemistry*, Volume 94, Issue 2, p404
- <sup>18</sup>D.I. Khomskii, (2005), *Journal of Magnetism and Magnetic Materials*, Vol. 306, p1-8
- <sup>19</sup>P.A. Cox, *Insulating Oxides*, In J.S. Rowlinson, M.L.H. Green, J. Halpern, S.V. Ley, T. Mukaiyama, R.L. Schowen, J.M. Thomas, A.H. Zewail, editors, *Transition Metal Oxides: An Introduction to Their Electronic Structure and Properties*, 1<sup>st</sup> Ed. (Paperback), Biddles Ltd., 1995, p149-153

- <sup>20</sup>P. Day, M.T. Hutchings, E. Janke, P.J. Walker, (1979), *Journal of the Chemical Society: Chemical Communications*, Issue 16, p711
- <sup>21</sup>G. Matsumoto, (1970), *Journal of the Physical Society of Japan*, Volume 23, Number 9, p606
- <sup>22</sup>E.O. Wollan, W.C. Koehler, (1955), *Physical Review*, Volume 100, Number 2, p545
- <sup>23</sup>C. Wang, J. Wang, Z. Gai, (2007), *Scripta Materiala*, Vol. 57, p789-792
- <sup>24</sup>E.C. Subbarao, (1962), *Journal of the American Ceramic Society*, Vol. 45, Iss. 4, p166
- <sup>25</sup>R.A. Armstrong, R.E. Newnham, (1972), *Material Research Bulletin*, Vol. 7, p1025
- <sup>26</sup>M. Tripathy, R. Mani, J. Gopalakrishnan, (2007), *Material Research Bulletin*, Vol. 42, p950
- <sup>27</sup>H. Hara, Y. Noguchi, M. Miyayama, (2004), *Key Engineering Materials*, Vol. 269, p27
- <sup>28</sup>B. Frit, J. Mercurio, (1992), *Journal of Alloys and Compounds*, Vol. 188, p27
- <sup>29</sup>J. Gopalakrishnan, A. Ramanan, C. Rao, D. Jefferson, D. Smith, (1984), *Journal of Solid State Chemistry*, Vol. 55, p101
- <sup>30</sup>M. Miyayama, (2006), *Journal of the Ceramic Society of Japan*, Vol. 114, Iss. 7, p583-589
- <sup>31</sup>A. Lisińska-Czejak, D. Czejak, M.J.M. Gomes, M.F. Kupriamov, (1999), *Journal of the European Ceramic Society*, Iss. 19, p969
- <sup>32</sup>M.M. Woolfson, *An Introduction to X-ray Crystallography*, 2<sup>nd</sup> Ed., Cambridge University Press, 1997
- <sup>33</sup>ICDD, <http://www.icdd.com/> , accessed 23/08/08
- <sup>34</sup>A.C. Larson and R.B. Von Dreele, (2000), *General Structure Analysis System (GSAS)*, Los Alamos National Laboratory Report LAUR 86-748
- B. H. Toby, (2001), EXPGUI, a graphical user interface for GSAS, *Journal Of Applied Crystallography*, Vol. 34, p210
- <sup>35</sup>ICSD, <http://cds.dl.ac.uk/cds/datasets/crys/icsd/llicsd.html> , accessed 23/08/08
- <sup>36</sup>H.M. Rietveld, (1967), *Acta Crystallographica*, Volume 22, p151
- <sup>37</sup>J. Crangle, *The Magnetic Properties of Solids*, 1<sup>st</sup> Ed., Edward Arnold: London, 1977
- <sup>38</sup>B.D. Josephson, (1962), *Physics Letters*, Vol. 1, Iss. 7, p251

- <sup>39</sup>J. Clarke, (1980), *IEEE Transactions on Electron Devices*, Vol. 27, Number 10, p1896
- <sup>40</sup>R.C. Jaklevic, J. Lambe, A.H. Silver, J.E. Mercereau, (1964), *Physical Review Letters*, Vol. 12, Number 7, p159
- <sup>41</sup>J.M. Ku, W.S. Ihl, K. Yong-Il, N. Seung-Hoon, (2004), *Journal of the Korean Physical Society*, Volume 45, p1240-1243
- <sup>42</sup>M. Garcia-Guaderrama, M.E Botello-Zubiate, A. Marquez-Lucero, J.A Matutes-Aquino, L.E. Fuentes-Cobas, (2004), *Revista Mexicana de Fisico*, Volume 50, p42-45
- <sup>43</sup>P. Lightfoot, C.H. Hervochoes, (2003), *Proceedings of the 10th International Ceramics Congress*, Volume 10, p623-630
- <sup>44</sup>J.G. Thompson, R.L. Withers, A.C. Willis, A.D. Rae, (1990), *Acta Crystallographica*, Volume B4, p474-487
- <sup>45</sup>Megaw H., (1973), *Crystal Structures*, London: W.B. Saunders, p. 216, 282
- <sup>46</sup>R.H. Mitchell, *Perovskites: Modern and Ancient*, 1<sup>st</sup> Ed., Almaz Press: Thunder Bay, 2002
- <sup>47</sup>X.W. Dong, K.F. Wang, J.G. Wan, J.S. Zhu, and J. Liu, (2008), *Journal of Applied Physics*, Volume 103
- <sup>48</sup>S. Zhang, Y. Chen, Z. Liu, N. Ming, J. Wang, G. Cheng, (2005), *Journal of Applied Physics*, Volume 97
- <sup>49</sup>A. Snedden, C.H. Hervochoes, P. Lightfoot, (2003), *Physical Review B*, Volume 67
- <sup>50</sup>S. Ahn, Y. Noguchi, M. Miyayama, T. Kudo, (2000), *Materials Research Bulletin*, Volume 35, p825-834
- <sup>51</sup>A. Srinivas, S.V. Suryanarayana, G.S. Kumar, M. Mahesh Kumar, (1999), *Journal of Physics: Condensed Matter*, Volume 11, p3335-3340
- <sup>52</sup>R.S. Singh, T. Bhimasankaram, G.S. Kumar, S.V. Suryanarayana, (1994), *Solid State Communications*, Volume 91, Issue 7, p567-569
- <sup>53</sup>C.H. Hervochoes, A. Snedden, R. Riggs, S.H. Kilcoyne, P. Manuel, P. Lightfoot, (2002), *Journal of Solid State Chemistry*, Volume 164, p280-291
- <sup>54</sup>D.F. Shriver, P.W. Atkins, *Inorganic Chemistry*, 3<sup>rd</sup> Ed., Oxford University Press, 1999
- <sup>55</sup>B. Shankar, H Steinfink, (1996), *Journal of Solid State Chemistry*, Volume 122, p390-393
- <sup>56</sup>E.E. McCabe, C. Greaves, (Received 2008), *Journal of Solid State Chemistry*, Awaiting Publication

<sup>57</sup>M.M. Kumar, A. Srinivas, G.S. Kumar, S.V. Suryanarayana, (1997), *Solid State Communications*, Volume 104, Number 12, p741-746

<sup>58</sup>S. Horiuchi, T. Kikuchi, M. Goto, (1977), *Acta Crystallographica Section A*, Volume 33, September Issue, p701

<sup>59</sup>R.L. Needs, S.E. Dann, M.T. Weller, J.C. Cherryman, R.K. Harris, (2005), *Journal of Materials Chemistry*, Volume 15, Issue 24, p2399-2407

## Appendix A

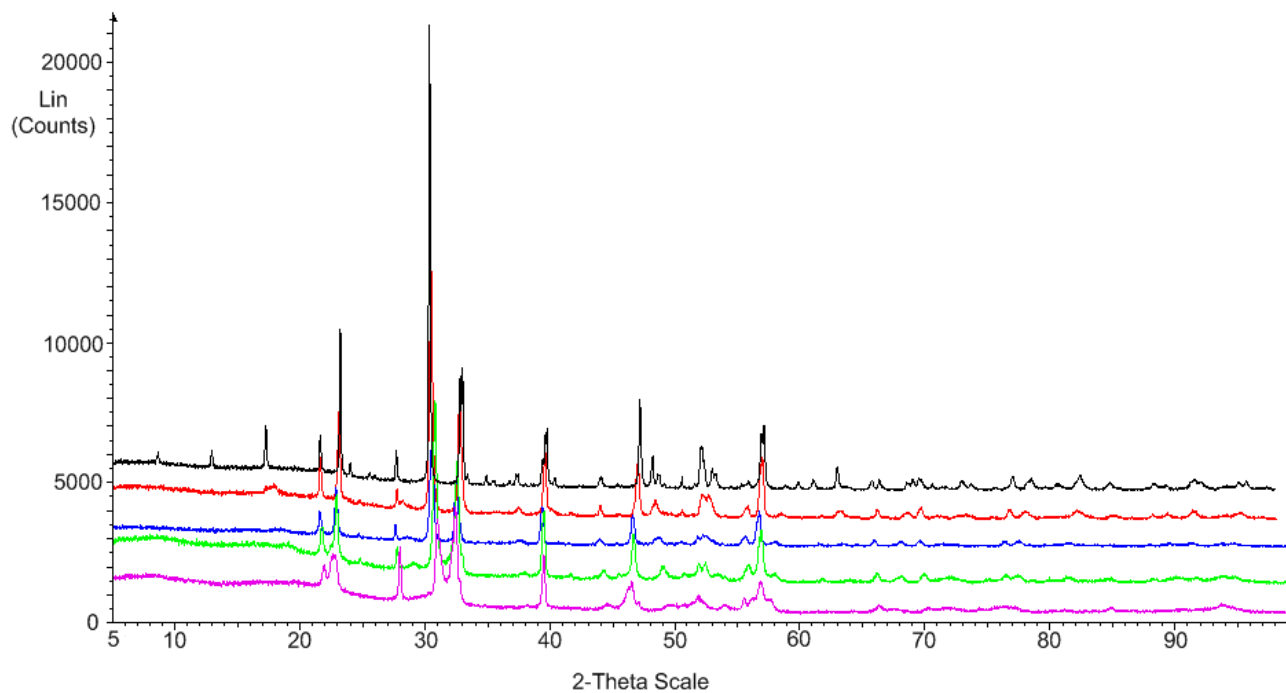


Figure 1: An example of peak shifting leading to convergence as the Fe content increases in  $\text{Bi}_5\text{Ti}_{1+x}\text{Fe}_{3-x}\text{O}_{15}$ .

### Scan Patterns from XRPD data

$\text{Bi}_5\text{FeTi}_3\text{O}_{15}$  Scan Pattern

$\text{Bi}_5\text{Fe}_{1.5}\text{Ti}_{2.5}\text{O}_{15}$  Scan Pattern

$\text{Bi}_5\text{Fe}_2\text{Ti}_2\text{O}_{15}$  Scan Pattern

$\text{Bi}_5\text{Fe}_{2.5}\text{Ti}_{1.5}\text{O}_{15}$  Scan Pattern

$\text{Bi}_5\text{Fe}_3\text{TiO}_{15}$  Scan Pattern

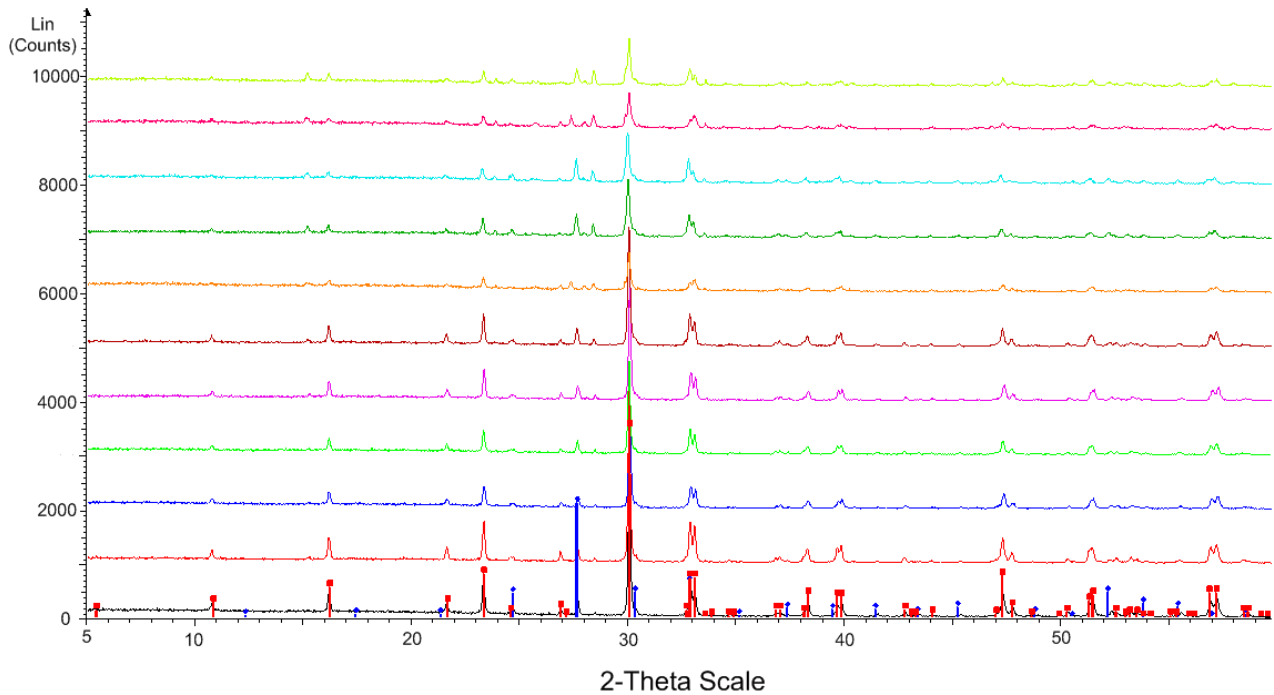


Figure 2: Comparison of XRPD data of attempted  $\text{Bi}_5\text{Mn}_{1+x}\text{Ti}_{3-x}\text{O}_{15}$  samples. The straight vertical lines show the calculated values of the phases suspected to comprise the samples.

**File Patterns from EVA Database**

$\text{Bi}_4\text{Ti}_3\text{O}_{12}$  File Pattern 73-2181

$\text{Bi}_{12}\text{MnO}_{20}$  File Pattern 82-1024

**Scan Patterns from XRPD data**

$\text{Bi}_5\text{MnTi}_3\text{O}_{15}$  Scan Pattern

$\text{Bi}_5\text{Mn}_{1.1}\text{Ti}_{2.9}\text{O}_{15}$  Scan Pattern

$\text{Bi}_5\text{Mn}_{1.2}\text{Ti}_{2.8}\text{O}_{15}$  Scan Pattern

$\text{Bi}_5\text{Mn}_{1.3}\text{Ti}_{2.7}\text{O}_{15}$  Scan Pattern

$\text{Bi}_5\text{Mn}_{1.4}\text{Ti}_{2.6}\text{O}_{15}$  Scan Pattern

$\text{Bi}_5\text{Mn}_{1.5}\text{Ti}_{2.5}\text{O}_{15}$  Scan Pattern

$\text{Bi}_5\text{Mn}_{1.6}\text{Ti}_{2.4}\text{O}_{15}$  Scan Pattern

$\text{Bi}_5\text{Mn}_{1.7}\text{Ti}_{2.3}\text{O}_{15}$  Scan Pattern

$\text{Bi}_5\text{Mn}_{1.8}\text{Ti}_{2.2}\text{O}_{15}$  Scan Pattern

$\text{Bi}_5\text{Mn}_{1.9}\text{Ti}_{2.1}\text{O}_{15}$  Scan Pattern

$\text{Bi}_5\text{Mn}_2\text{Ti}_2\text{O}_{15}$  Scan Pattern

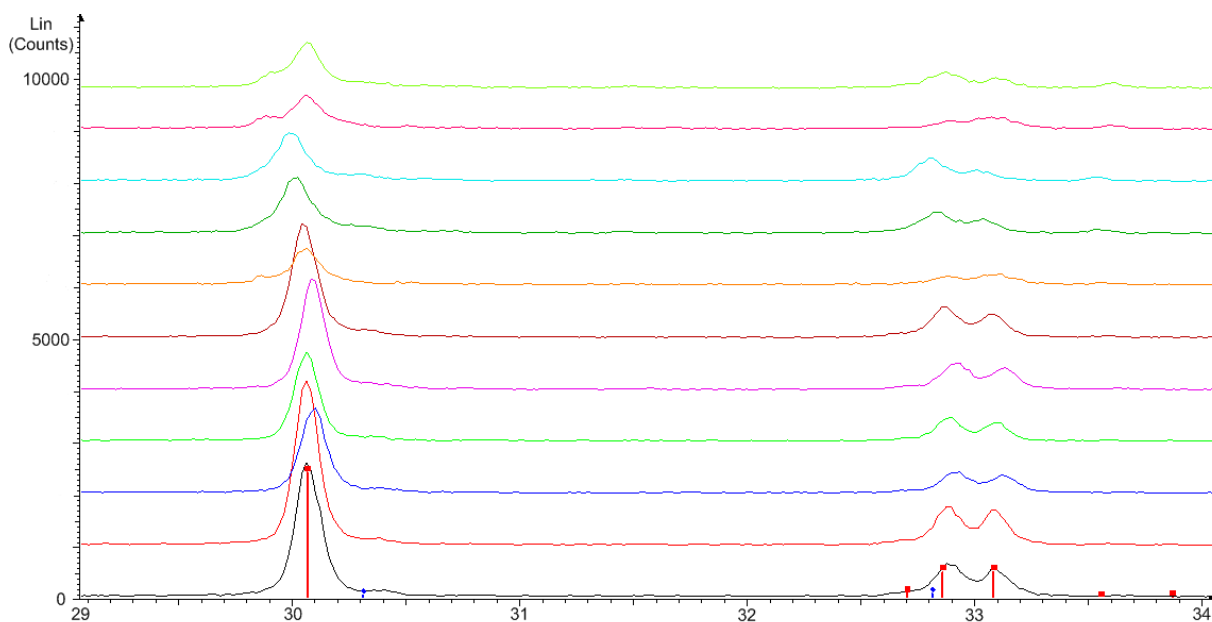


Figure 3: Close up of the XRPD data of attempted  $\text{Bi}_5\text{Mn}_{1+x}\text{Ti}_{3-x}\text{O}_{15}$  samples. The straight vertical lines show the calculated values of the phases suspected to comprise the samples.

#### **File Patterns from EVA Database**

$\text{Bi}_4\text{Ti}_3\text{O}_{12}$  **File Pattern** 73-2181

$\text{Bi}_{12}\text{MnO}_{20}$  **File Pattern** 82-1024

#### **Scan Patterns from XRPD data**

$\text{Bi}_5\text{MnTi}_3\text{O}_{15}$  Scan Pattern

$\text{Bi}_5\text{Mn}_{1.1}\text{Ti}_{2.9}\text{O}_{15}$  **Scan Pattern**

$\text{Bi}_5\text{Mn}_{1.2}\text{Ti}_{2.8}\text{O}_{15}$  **Scan Pattern**

$\text{Bi}_5\text{Mn}_{1.3}\text{Ti}_{2.7}\text{O}_{15}$  **Scan Pattern**

$\text{Bi}_5\text{Mn}_{1.4}\text{Ti}_{2.6}\text{O}_{15}$  **Scan Pattern**

$\text{Bi}_5\text{Mn}_{1.5}\text{Ti}_{2.5}\text{O}_{15}$  **Scan Pattern**

$\text{Bi}_5\text{Mn}_{1.6}\text{Ti}_{2.4}\text{O}_{15}$  **Scan Pattern**

$\text{Bi}_5\text{Mn}_{1.7}\text{Ti}_{2.3}\text{O}_{15}$  **Scan Pattern**

$\text{Bi}_5\text{Mn}_{1.8}\text{Ti}_{2.2}\text{O}_{15}$  **Scan Pattern**

$\text{Bi}_5\text{Mn}_{1.9}\text{Ti}_{2.1}\text{O}_{15}$  **Scan Pattern**

$\text{Bi}_5\text{Mn}_2\text{Ti}_2\text{O}_{15}$  **Scan Pattern**

## **Appendix B: Mössbauer Spectroscopy**

### The Mössbauer Effect

Mössbauer spectroscopy is an analytical technique that is used to determine the magnetic and time-dependent properties of a material by the effects of recoilless gamma ray emission and absorption. The Mössbauer effect is based on the resonant absorption of gamma rays in crystalline structures.

A nuclei can occupy a variety of energy levels, and it is possible to split or alter these energy levels based on the surrounding electronic and magnetic environment, however these hyperfine interactions with the environment of the nuclei are extremely small and difficult to observe. In a variety of different circumstances, transitions between different energy levels can be caused or evidenced by the absorption or emission of a gamma ray.

A free nucleus will undergo a certain degree of recoil in order to conserve momentum, when absorbing or emitting a gamma ray. A gamma ray that is absorbed and then subsequently emitted will have less energy, because the recoil of the nucleus results in an overall loss of kinetic energy. The recoil effect means that there is no resonance of nuclei, the loss of kinetic energy due to the conservation of momentum needs to be overcome to provide useful resonance effects.

A resonant signal is important because individual nuclei will be moving in random directions, giving the gamma ray a variety of different energy values based on the Doppler effect. Overlap between different signals leads to resonance, but with freely moving nuclei this effect is low because at most only a millionth of the gamma rays have overlapping signals, making this technique impractical for detecting hyperfine interactions.

However in 1957, Ernst Mössbauer discovered what would be known as the Mössbauer Effect. When a gamma ray is absorbed by a nucleus in a crystal lattice the recoiling effect is massively limited as the mass of the entire lattice is much greater than the mass of a single nucleus. As the recoil of the lattice approaches zero, the difference in energy between absorbed and emitted gamma rays approaches zero. At zero, the gamma ray absorbed and the gamma ray emitted have the same energy, and resonance is achieved.

In a cubic environment, if the absorbing and emitting nuclei are identical, then the spectrum will show a single absorption line. An excited energy level for a nucleus has a finite lifetime before a gamma ray is emitted. The average lifetime of an excited state prior to gamma ray emission determines the linewidth of the spectrum. As the natural linewidth of the most commonly used Mössbauer isotope,  $^{57}\text{Fe}$  is approximately  $5 \times 10^{-9}$  eV, whereas Mössbauer gamma rays have an energy of 14.4 keV. This difference, of 12 orders of magnitude, gives resolution sufficient to detect

the hyperfine interactions of the nucleus.

### Mössbauer Spectroscopy

By oscillating a radioactive source towards and away from the target material at a low velocity ( a few millimetres per second), the Doppler effect leads to an energy shift of the gamma ray. This energy shift is minute enough to observe the hyperfine interactions. The oscillating effect also allows for slight incremental modulation of the gamma ray.

When you get resonant absorption of the gamma ray, i.e. when the gamma ray energy matches an energy level transition of the sample material, you can see a peak in the spectra. Obviously, the sample has to be thin enough to allow the gamma rays to pass through. The energy levels of the absorbing nuclei are altered by their environment in three main ways, namely, isomer shift, magnetic splitting and quadrupole splitting.

Differences between the s-electron environments of the source and the receiver produces a shift in the resonance energy. The shift in transition energy, caused by this difference in electron charge density, is what is known as isomer shift. This shift is relative to a known absorption, it cannot be measured directly. Isomer shift is particularly useful for determination of valency state as ferrous ions have larger positive shifts than ferric ions. This is because ferrous ions have less influence from the s-electrons at the nucleus due to the screening effects of the greater number of d-electrons. The formula for calculating isomer shift is given by the formula below<sup>1</sup>:

$$\delta = \left( \frac{Ze^2 R^2 c}{5 \epsilon_0 E_\gamma} \right) [\rho_a(0) - \rho_s(0)] \left[ \frac{\Delta R}{R} \right] \text{ mm s}^{-1}$$

Where  $Z$  is the atomic number,  $e$  is the electronic charge,  $R$  is the effective nuclear radius,  $c$  is the speed of light,  $E_\gamma$  is the energy of the Mössbauer gamma ray, the  $\rho_a(0)$  and  $\rho_s(0)$  terms are the total electron densities at the nucleus for absorber and source, respectively and  $\Delta R = R_{excited} - R_{ground}$ .

Magnetic splitting is a result of Zeeman splitting, the dipolar interaction with a magnetic field experienced by the nuclear spin moment. The magnetic field experienced by the nucleus is given by:

$$B_{eff} = (B_{contact} + B_{dipolar} + B_{orbital}) + B_{applied}$$

As you can see the effective magnetic field is the total combination of the atoms own forces (in brackets) and an applied magnetic field.  $B_{contact}$  is the result of spin on the electrons that are

responsible for polarisation of spin density at the nucleus.  $B_{dipolar}$  represents the dipolar field of those electrons, while  $B_{orbital}$  represents their orbital moment.

For nuclear states with an angular momentum quantum number  $l$  greater than 0 degeneracy is increased. In these circumstances, the magnetic field splits the nuclear level into  $2l+1$  substates. As transitions only occur when the difference in  $m_l$  between the ground state and the excited state is either 0 or 1, this gives six different transitions, and therefore six different lines.

The positions that the split line takes are proportional to the splitting of the energy levels. Their intensities however, are related to the angle between the nuclear spin moment and the Mössbauer gamma ray. The relative intensities are given in the following proportions for a sextuplet<sup>ii</sup>:

$$3: \frac{4 \sin^2 \theta}{1 + \cos^2 \theta} : 1:1: \frac{4 \sin^2 \theta}{1 + \cos^2 \theta} : 3$$

Meaning that the two outermost and two innermost lines always follow the same relationship, but the intensities of the second and fourth lines depend entirely on the angle between the nuclear spin moment and the Mössbauer gamma ray. Typically, in a polycrystalline sample with no applied field the average intensity is approximately 2, but in a single crystal or applied field, this value can be anything between 0 and 4.

Quadrupole splitting occurs due to the non-spherical distribution of charge in nuclei that have an  $l$  (angular quantum momentum number, as before) that is greater than a half. This produces a nuclear quadrupole moment which splits energy levels in the presence of an asymmetrical electrical field. An asymmetric electric field typically occurs in situations with asymmetric electronic charge distribution or possibly by ligand arrangement. The equation for calculation of electric field gradient is as follows<sup>i</sup>:

$$V_{zz} = \frac{1}{4\pi\epsilon_0} \sum_i q_i r_i^{-3} (3\cos^2\theta_i - 1)$$

The magnitude of quadrupole splitting is related to both the electric field gradient and the quadrupole moment,  $Q$ , giving:

$$\Delta = eQV_{zz}$$

Alone or in combination, isomer shift, magnetic splitting and quadrupole splitting are characteristics of Mössbauer spectra which can tell us a great deal about the samples under observation.

For example, the appearance of an isomer shift between two different Mössbauer spectra,

taken before and after calcination, can be indicative of a second compound with a different oxidation state being formed. Similarly, if an atom moves from its central position in a unit cell there will be a corresponding change in the electronic charge distribution, making it asymmetric and therefore leading to quadrupole splitting. Obviously, the property indicated by magnetic splitting is a display of whether or not a sample is magnetically ordered.

- i R.V. Parish, *Mössbauer Spectroscopy and the Chemical Bond*; In: D.P.E. Dickson, F.J. Berry, editors, *Mössbauer Spectroscopy*, 1<sup>st</sup> Ed., Cambridge University Press, 1986, p21
- ii M.F. Thomas, C.E. Johnson, *Mössbauer Spectroscopy of Magnetic Solids*; In: D.P.E. Dickson, F.J. Berry, editors, *Mössbauer Spectroscopy*, 1<sup>st</sup> Ed., Cambridge University Press, 1986, p152